EUROPEAN ORGANIZATION FOR NUCLEAR RESEARCH (CERN)

CERN-EP-2022-039
2023/11/25

CMS-HIG-21-010

Search for a charged Higgs boson decaying into a heavy neutral Higgs boson and a W boson in proton-proton collisions at $\sqrt{s} = 13\,\text{TeV}$

The CMS Collaboration

Abstract

A search for a charged Higgs boson $H^{\pm}$ decaying into a heavy neutral Higgs boson H and a W boson is presented. The analysis targets the H decay into a pair of tau leptons with at least one of them decaying hadronically and with an additional electron or muon present in the event. The search is based on proton-proton collision data recorded by the CMS experiment during 2016–2018 at $\sqrt{s} = 13\,\text{TeV}$, corresponding to an integrated luminosity of $138\,\text{fb}^{-1}$. The data are consistent with standard model background expectations. Upper limits at 95% confidence level are set on the product of the cross section and branching fraction for an $H^{\pm}$ in the mass range of 300–700 GeV, assuming an H with a mass of 200 GeV. The observed limits range from 0.085 pb for an $H^{\pm}$ mass of 300 GeV to 0.019 pb for a mass of 700 GeV. These are the first limits on $H^{\pm}$ production in the $H^{\pm} \to HW^{\pm}$ decay channel at the LHC.

Submitted to the Journal of High Energy Physics

1 Introduction

The experimental confirmation of the Brout–Englert–Higgs mechanism [1–6] at the CERN LHC [7–9] has provided the long-sought solution to the electroweak symmetry breaking problem. It has also further established the standard model (SM) of particle physics as a successful theory. Subsequent precision measurements of the couplings of the observed Higgs boson with the SM particles are in agreement with expectations, with an experimental precision of ≈5–33% [10–13]. Regardless of the success it has achieved, the SM is still considered to be an effective field theory valid only at low energies because of its inability to address various fundamental theoretical problems and compelling observations in nature such as the naturalness problem, the vacuum metastability, the conjectured cosmological inflation, and the matter-antimatter asymmetry of our universe.

Numerous theoretical models have been proposed to remedy the shortcomings of the SM, many of which predict that the Higgs sector must also be extended. Minimal extensions known as two-Higgs-doublet models (2HDMs) [14–17] include a second complex doublet and are classified into four types according to the couplings of the Higgs doublets to fermions. The two-doublet structure gives rise to five physical Higgs bosons via spontaneous symmetry breaking: two neutral CP-even particles h and H with $m_{\mathrm{h}} \leq m_{\mathrm{H}}$, one neutral CP-odd particle A, and two charged Higgs bosons $\mathrm{H}^{\pm}$. In these models the ratio of the vacuum expectation values of the two Higgs doublets, $\tan\beta$, and the mixing angle, α, between h and H are free parameters. These can be tuned to the alignment limit $\sin(\beta-\alpha)=1$ whereby h aligns with the properties of the SM Higgs boson with m_{h} = 125 GeV [18], while the additional Higgs bosons may appear at the TeV scale or below it [19].

Three mass regions are conveniently defined for the classification of charged Higgs bosons: light ($m_{\mathrm{H}^{\pm}} < m_{\mathrm{t}} - m_{\mathrm{b}}$), intermediate ($m_{\mathrm{H}^{\pm}} \approx m_{\mathrm{t}}$), and heavy ($m_{\mathrm{H}^{\pm}} > m_{\mathrm{t}} + m_{\mathrm{b}}$), where $m_{\mathrm{H}^{\pm}}$, m_{t}, and m_{b} represent the masses of the charged Higgs boson, the top and bottom quarks, respectively. The search described in this paper is focused on a heavy $\mathrm{H}^{\pm}$, whose production at the LHC would take place predominantly in association with top and bottom quarks. The associated top quark production dominates and can be described in the four- and five-flavor scheme (4FS and 5FS), which yield consistent results at sufficiently high order of perturbation theory [20]. The corresponding leading-order (LO) Feynman diagrams are shown in Fig. 1, with charge-conjugate processes implied.

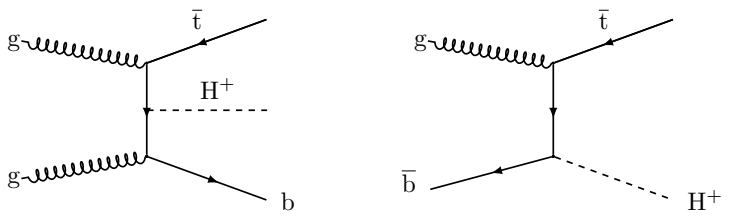

Figure 1: Leading order Feynman diagrams for the production of a heavy H^{+} at the LHC through $\mathrm{pp} \to \mathrm{t(b)H}^{+}$ in the 4FS (left) and 5FS (right).

When considering 2HDMs, the decay branching fractions $\mathcal{B}$ of $\mathrm{H}^{\pm}$ can vary significantly between different models. Under the enforcement of the Z2 symmetry there are four types of 2HDMs which, for $\tan\beta = 1$, lead to the channels $\mathrm{H}^{\pm} \to \tau^{\pm}\nu_{\tau}$ and $\mathrm{H}^{\pm} \to \mathrm{cs}$ being dominant in the light-$\mathrm{H}^{\pm}$ region. In the heavy-$\mathrm{H}^{\pm}$ region, the decay mode $\mathrm{H}^{\pm} \to \mathrm{tb}$ dominates, with some competition from the $\mathrm{H}^{\pm} \to \mathrm{hW}^{\pm}$ and $\mathrm{H}^{\pm} \to \mathrm{HW}^{\pm}$ decay modes. This behavior also holds in the alignment limit with the only difference being that $\mathcal{B}(\mathrm{H}^{\pm} \to \mathrm{HW}^{\pm})$ increases

faster with $m_{H^\pm}$, while $\mathcal{B}(H^\pm \to hW^\pm)$ vanishes completely. At larger values of $\tan\beta$, the interplay between the channels $H^\pm \to HW^\pm$ and $H^\pm \to hW^\pm$ becomes more intricate, with the former becoming important once kinematically attainable and the latter dominating because of the large phase space available.

The importance of the potential interference between the $H^\pm \to HW^\pm$ and $H^\pm \to hW^\pm$ channels is difficult to quantify as it highly depends on the considered parameter space. In general, however, a large $H^\pm \to hW^\pm$ coupling is always associated with a small $H^\pm \to HW^\pm$ coupling, and vice versa. As discussed in Ref. [21], assuming a misalignment of $\approx$0.1 with $\sin(\beta-\alpha) = 0.9$, $\mathcal{B}(H^\pm \to hW^\pm)$ is suppressed by a factor of $\approx$100 with respect to $\mathcal{B}(H^\pm \to HW^\pm)$, while the interference between $H^\pm \to HW^\pm$ and $H^\pm \to hW^\pm$ is also expected to be suppressed by at least a factor of $\approx$10 compared to the contribution from $H^\pm \to HW^\pm$ itself. In this paper, we focus on the $H^\pm \to HW^\pm$ decay mode and neglect completely the $H^\pm \to hW^\pm$ decay mode, as well as their interference. For the neutral Higgs boson, typically the most frequent final states close to the alignment limit are the bb and $\tau\tau$, while the WW, ZZ, and $\gamma\gamma$ channels are experimentally the cleanest ones. However, the aforementioned decay rates are model-dependent and are affected, directly or indirectly, by the value of m_H.

Since no charged scalar boson exists in the SM, a discovery of a charged Higgs boson would provide unequivocal proof of physics beyond the SM. To date, various searches for an $H^\pm$ signature have been conducted by the ATLAS and CMS Collaborations in proton-proton (pp) collisions at $\sqrt{s} = 7$, 8, and 13 TeV. Searches for a light $H^\pm$ include the channels $H^\pm \to \tau^\pm\nu_\tau$ [22–25], $H^\pm \to cs$ [26, 27], $H^\pm \to cb$ [28], and $H^\pm \to W^\pm A$ [29]. In the heavy-$H^\pm$ region, the searches include the channels $H^\pm \to tb$ [23, 30–32] and $H^\pm \to \tau^\pm\nu_\tau$ [22–24, 33, 34]. Charged-current processes from low-energy flavor observables, such as tauonic B meson decays and the $b \to s\gamma$ transition, have yielded indirect lower limits on $m_{H^\pm}$ [35, 36]. Searches for $H^\pm \to W^\pm Z$ decays predicted in Higgs triplet models [37–39] have also been conducted in the vector boson (V = Z or W) fusion production mode [40–43]. Finally, the ATLAS Collaboration has set limits on $H^\pm$ production with a search for dijet resonances in events with an isolated charged lepton [44]. No evidence of a charged Higgs boson has been reported in any of the aforementioned searches. Searches for additional heavy neutral Higgs bosons have also been performed at experiments at LEP [45] and the Tevatron [46–49]. These are superseded by searches performed by the ATLAS and CMS Collaborations in the bb [50–53], $\mu\mu$ [54–57], and $\tau\tau$ [54, 58–65] final states.

In this paper, a direct search for a heavy $H^\pm$ is performed through the $H^\pm \to HW^\pm$ and $H \to \tau\tau$ decay modes, targeting the $H^\pm \to HW^\pm$ decay channel for the first time at the LHC. In this search it is assumed that the H boson has a mass of $m_H = 200$ GeV. This particular choice appears as a benchmark point in various scenarios such as extended Inert Doublet Models aiming to provide a viable Dark Matter candidate [66, 67], in 2HDM frameworks with new sources of CP-violation [68] or a strong first order electroweak phase transition [69] which are needed for a successful electroweak baryogenesis. Such heavy neutral scalars have also been proposed to address flavor puzzles such as the anomalous magnetic moment of the muon [70].

The search focuses on an associated $H^\pm$ production with a hadronically decaying top quark, in final states with at least one tau lepton decaying hadronically (τ_h) and exactly one isolated lepton (ℓ = e, μ), as shown in Fig. 2. Four distinct final states are targeted: $e\tau_h$, $\mu\tau_h$, $e\tau_h\tau_h$, and $\mu\tau_h\tau_h$. For the $\ell\tau_h$ final states, candidate events contain one τ_h candidate, one isolated lepton, missing transverse momentum ($\vec{p}_T^{\,miss}$), and three additional hadronic jets from W boson decays andb quarks. The $\ell\tau_h$ search employs a multivariate analysis (MVA) classifier based on boosted decision tree with gradient boost (BDTG) to distinguish the signal from backgrounds.

For the $\ell\tau_h\tau_h$ final states, candidate events are selected by requiring one additional τ_h candidate and by relaxing the hadronic jet multiplicity requirement to at least two. In these final states, the transverse mass of the charged Higgs boson, m_T, is used to distinguish signal from backgrounds. Upper limits on the product of the $H^\pm$ production cross section, $\sigma_{H^\pm}$, and the branching fraction $\mathcal{B}(H^\pm \to HW^\pm, H \to \tau\tau)$ for the decay chain $H^\pm \to HW^\pm$ with $H \to \tau\tau$, are presented as functions of $m_{H^\pm}$.

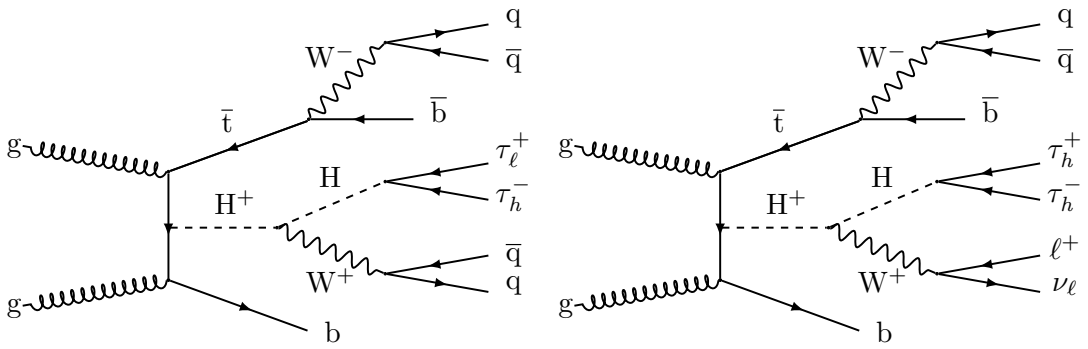

Figure 2: Feynman diagrams showing the signal processes targeted by this analysis, with the production of a heavy H^+ in the 4FS, followed by the $H^+ \to HW^+$ and $H \to \tau\tau$ decays, resulting in $\ell\tau_h$ (left) and $\ell\tau_h\tau_h$ (right) final states. Contributions to the $\ell\tau_h$ final state may also arise from the right diagram when one τ_h from the $H \to \tau\tau$ decay is not reconstructed.

The paper is organized as follows. A brief description of the CMS detector is given in Section 2, while the collision data and simulated samples are discussed in Section 3. Section 4 describes the global event reconstruction and physics object identification, followed by the event selection in Section 5. Background estimation, search strategy, and systematic uncertainties are described in Sections 6, 7, and 8, respectively. Finally, the results are presented in Section 9 and summarized in Section 10.

2 The CMS detector

The central feature of the CMS apparatus is a superconducting solenoid of 6 m internal diameter, providing a magnetic field of 3.8 T. Within the solenoid volume are a silicon pixel and strip tracker, a lead tungstate crystal electromagnetic calorimeter (ECAL), and a brass and scintillator hadron calorimeter, each composed of a barrel and two endcap sections. Forward calorimeters extend the pseudorapidity (η) coverage provided by the barrel and endcap detectors up to $|\eta| = 5$. Muons are detected in gas-ionization chambers embedded in the steel flux-return yoke outside the solenoid.

Events of interest are selected using a two-tiered trigger system. The first level, composed of custom hardware processors, uses information from the calorimeters and muon detectors to select events at a rate of around 100 kHz within a time interval of less than 4 μs [71]. The second level, known as the high-level trigger (HLT), consists of a farm of processors running a version of the full event reconstruction software optimized for fast processing, and reduces the event rate to around 1 kHz before data storage [72].

A more detailed description of the CMS detector, together with a definition of the coordinate system used and the relevant kinematic variables, can be found in Ref. [73].

3 Collision data and simulated samples

The analysis presented in this paper uses pp collision data collected with the CMS experiment at $\sqrt{s} = 13\,\text{TeV}$ during the years 2016, 2017, and 2018. The corresponding integrated luminosities are 36.3, 41.5, and 59.8 fb^{-1}, respectively, amounting to a total of 138 fb^{-1}. The aforementioned data were collected with the use of single-electron and single-muon triggers with isolation criteria. The trigger thresholds are mentioned in Section 5.

Simulated events are used to model the signal and background processes using various Monte Carlo (MC) event generators. The signal samples are generated with the MADGRAPH5_aMC@NLO generator [74] v2.2.2 for 2016 (v2.4.2 for 2017–2018) using the 4FS at next-to-LO (NLO) precision in quantum chromodynamics (QCD). The decays of the $\text{H}^{\pm}$ resonances are generated with MADSPIN [75] to preserve spin-correlation and finite-width effects. Both charge-conjugate signal processes are generated with four mass hypotheses $m_{\text{H}^{\pm}} = 300$, 400, 500, and 700 GeV and under the assumption that $m_{\text{h}} = 125\,\text{GeV}$ and $m_{\text{H}} = 200\,\text{GeV}$.

The top quark-antiquark pair ($\text{t}\bar{\text{t}}$) production constitutes an important background that contributes significantly to all final states considered. It is simulated with NLO precision in QCD using the POWHEG v2.0 [76–81] generator. Its cross section is obtained from the TOP++ v2.0 [82] calculation that includes next-to-NLO (NNLO) corrections in QCD and resummation of the next-to-next-to-leading logarithmic soft-gluon terms. Other important sources of background include single top quark production (single t), $\text{t}\bar{\text{t}}\text{X}$ with $\text{X} = \text{W}, \text{Z}, \text{h}$, or $\text{t}\bar{\text{t}}$, and electroweak processes including V+jets with $\text{V} = \text{Z}$ or Wand diboson (WZ, ZZ, WW) production. For the single t samples, the *t*-channel process is generated with POWHEG v2.0 at NLO precision in QCD using the 4FS [83] and interfaced with MADSPIN for simulating the top quark decay. The *s*-channel process is simulated using MADGRAPH5_aMC@NLO, while the production via the tW-channel is simulated at NLO in QCD using the 5FS and POWHEG v2.0 [84]. The production of $\text{t}\bar{\text{t}}$ in association with W or Z boson is simulated with NLO precision in QCD using MADGRAPH5_aMC@NLO. The $\text{t}\bar{\text{t}}\text{h}$ background process is generated using POWHEG v2.0 at NLO [85], with a Higgs boson mass of 125 GeV. The top quark mass is set to $m_{\text{t}} = 172.5\,\text{GeV}$. The V+jets samples are generated at LO precision using MADGRAPH5_aMC@NLO, with up to four partons included in the matrix element (ME) calculations. Finally, the diboson processes are generated at LO precision using PYTHIA v8.212 [86] .

For processes generated at LO precision in QCD, the MLM matching and merging procedure is used [87], whereby partons from the ME calculation are matched to the jets reconstructed after the perturbative shower. For processes generated at NLO precision in QCD with the MADGRAPH5_aMC@NLO generator, the events from the ME characterized by different parton multiplicities are merged with the FxFx procedure [88]. The matching between the ME calculation and the parton shower in POWHEG v2.0 is controlled by the damping factor h_{damp}, which has a value set to $h_{\text{damp}} = 1.379 m_{\text{t}}$. It is used to limit the resummation of higher-order effects by the Sudakov form factor to below a given p_{T} scale.

For the generation of the above-mentioned simulated processes, the parton distribution functions (PDFs) are parameterized using NNPDF3.0 [89] for 2016 (NNPDF3.1 [90] for 2017–2018). The PDFs in the ME calculations are at NLO for NNPDF3.0 and at NNLO for NNPDF3.1. The parton shower and fragmentation are modeled with the PYTHIA generator v8.212 for 2016 samples (v8.230 for 2017–2018). The PYTHIA parameters affecting the description of the underlying event are set to the CUETP8M1 tune [91] for 2016 (CP5 tune [92] for 2017–2018). The response of the CMS detector is simulated using GEANT4 v9.4 [93] and reconstructed using the same version of the CMS software as that used for the collision data.

The effect of additional inelastic pp interactions within the same or nearby bunch crossings, henceforth referred to as pileup, is taken into account by generating concurrent minimum bias events. All simulated events are weighted to match the pileup distributions observed in the data. The average number of pileup in the 2016 data set was 23, increasing to 32 during the 2017–2018 data taking.

4 Object reconstruction

The global event reconstruction is based on the particle-flow (PF) algorithm [94], which uses an optimized combination of information from the elements of the CMS detector to reconstruct individual particles in an event. It categorizes these PF candidates as photons, electrons, muons, charged hadrons, and neutral hadrons. Higher-level objects are reconstructed from combinations of the PF candidates. The primary pp interaction vertex (PV) is taken to be the vertex corresponding to the hardest scattering in the event, evaluated using tracking information alone. More specifically, the individual tracks originating from the same candidate vertex are clustered using the anti-k_T algorithm with a distance parameter of 0.4 [95], as implemented in the FASTJET library [96]. For each PV candidate the $\sum p_T^2$ value is computed by considering the clustered jets, the remaining single tracks, and the neutral particle contributions inferred from the negative vector sum of the p_T of those jets. The PV with the largest $\sum p_T^2$ is chosen as the one corresponding to the hard scattering. All other candidate vertices are attributed to pileup, with the exception of secondary vertices that are transversely displaced from the PV and indicative of decays of long-lived particles emerging from it.

Electrons are identified as charged-particle tracks that are potentially associated with ECAL energy clusters and bremsstrahlung photons emitted while traversing the tracker material. Their momentum is estimated by combining the energy measurement in the ECAL with the momentum measurement in the tracker. The momentum resolution for electrons with $p_T \approx 45\,\text{GeV}$ from $Z \to ee$ decays ranges from 1.7 to 4.5%. It is generally better in the barrel region than in the endcaps, and also it depends on the bremsstrahlung energy emitted by the electron as it traverses the material in front of the ECAL. An MVA discriminant [97] is used to achieve better discrimination of prompt isolated electrons from other electron candidates, mainly originating from photon conversions, jet misidentification, and semileptonic b hadron decays. It requires as input several variables describing the shapes of the energy deposits in the ECAL and the track quality. In this paper, a medium (loose) working point with an identification efficiency of 90 (>99)% is used for selecting (vetoing) electrons, corresponding to a rate of jets misidentified as electrons of ≈1 (20)%.

Muons are reconstructed as tracks in the central tracker consistent with either a track or several hits in the muon system, and associated with calorimeter deposits compatible with the muon hypothesis. They are measured in the range of $|\eta| < 2.4$, with detection planes using three technologies: drift tubes, cathode strip chambers, and resistive plate chambers. Their momentum is obtained from the curvature of the corresponding tracks in the silicon tracker, with a relative resolution of 1 and 3% for muons with p_T up to 100 GeV in the barrel and endcaps, respectively. The p_T resolution in the barrel is better than 7% for muons with p_T up to 1 TeV [98]. To increase the purity of prompt muons originating at the PV, a set of discriminants is employed based on the track fit quality, the number of hits per track, and the degree of compatibility of the information from the tracker and muon systems. A tight (loose) working point with an efficiency of ≈95 (99)% is used for selecting (vetoing) muons, in order to suppress muons from decays in flight and misidentified muons from hadronic punch-through.

Both prompt and displaced reconstructed leptons are used in this analysis, with the latter ex-

clusively used in the validation of the background estimation, described in detail in Section 6. In both cases the background contributions from misidentified leptons are further suppressed by applying stringent requirements on the lepton isolation. The relative lepton isolation variable I_{rel} is employed to ensure that the leptons are not associated with any significant electromagnetic or hadronic activity in the detector. It is defined as the scalar p_{T} sum, normalized to the lepton p_{T}, of all PF candidates within a cone of radius $\Delta R = \sqrt{(\Delta\eta)^2 + (\Delta\phi)^2} < 0.3$ (0.4) around the electron (muon) direction at the PV, where ϕ is the azimuthal angle in radians. The lepton itself is excluded from the calculation. To mitigate any effects due to contamination from pileup, only PF candidates whose tracks are associated with the PV are taken into account. For neutral hadrons and photons, where the absence of an associated track precludes an unambiguous association with the PV, an estimate of the pileup contribution is subtracted from their energy sums [99]. A tight (loose) isolation criterion with discriminant $I_{\text{rel}} < 0.15$ (0.25) is used in lepton selection (veto). The three-dimensional impact parameter significance, which is the impact parameter value normalized to its uncertainty, can also be used to further suppress electrons from photon conversions and muons originating from in-flight decays of hadrons. Its value is required to be less than ten for prompt electrons, or greater than three for all displaced electrons or muons.

Jets are reconstructed from PF candidates using the anti-k_{T} algorithm [95], as implemented in the FASTJET package [96], with a distance parameter of 0.4. The jet momentum is determined as the vectorial sum of all particle momenta in the jet. It is found from simulation to be within 5–10% of the true momentum, over the whole p_{T} spectrum and detector acceptance. Pileup can contribute additional tracks and calorimetric energy depositions, increasing the apparent jet momentum. To mitigate this effect, tracks identified to be originating from pileup vertices are discarded and an offset correction is applied to correct for remaining contributions [99]. Jet energy corrections are derived from simulation studies so that the average measured energy of jets becomes identical to that of particle-level jets. In situ measurements of the momentum balance in dijet, photon+jet, Z+jet, and multijet events are used to determine any residual differences between the jet energy scale in data and in simulation, and appropriate corrections are applied to simulated events [100]. After the corrections, the jet energy resolution amounts typically to 15–20% at 30 GeV, 10% at 100 GeV, and 5% at 1 TeV [100].

The identification of jets that originate from the hadronization of b quarks (b jets) is performed with the DEEPJET multiclass flavor-tagging algorithm, as described in Refs. [101–103]. In this analysis, a medium working point of this algorithm is chosen that corresponds to a b-jet identification efficiency of ≈80%. The associated misidentification rate for jets originating from light quarks and gluons (c quarks) is 1 (15)% [102].

The τ_{h} candidates are reconstructed with the hadrons-plus-strips algorithm, as described in Ref. [104]. It uses clustered anti-k_{T} jets as seeds to reconstruct τ decay modes with one charged hadron and up to two neutral pions (one-prong), or three charged hadrons and up to one neutral pion (three-prong). The neutral pions, which decay promptly to a photon pair, are reconstructed as strips of p_{T}-dependent size in the η-ϕ plane from reconstructed electrons and photons contained in the jet. These strips are narrow in η but wide in ϕ to allow for the broadening of ECAL energy deposits due to photon conversions. The τ_{h} decay mode is then obtained by combining the charged hadrons with the strips, resulting in a reconstruction efficiency of ≈80%. To efficiently discriminate the τ_{h} decays against jets originating from the hadronization of quarks or gluons, and against electrons or muons, the DEEPTAU [105, 106] multiclass τ identification algorithm is used. It exploits the reconstructed event quantities by combining low-level information from the tracking, calorimeter, and muon detectors with high-level properties of the τ_{h} candidate and other PF candidates in its vicinity. The multiclassification output

y_α represents a Bayesian probability that the τ_h candidate originates from a lepton ($\alpha = e, \mu$), the hadronization of a quark or gluon ($\alpha = j$), or a genuine τ_h ($\alpha = \tau$). The aforementioned output enables the definition of three discriminators according to the ratio $D_\alpha = y_\tau / (y_\tau + y_\alpha)$ with $\alpha = e, \mu, j$. For this analysis, medium and tight working points of D_e and D_μ are used with efficiencies of 62 and 70% and misidentification rates of 0.2 and 0.03%, respectively. For D_j, the medium and loose working points are used with efficiencies of 49 and 70% for misidentification rates of 0.4 and 5%, respectively, for τ_h candidates with p_T up to 200 GeV. The selected τ_h candidates that pass the loose but fail the medium D_j working point are referred to as anti-isolated τ_h's and are solely used in the background estimation as described in Section 6.

The $\vec{p}_T^{\,miss}$ is computed as the negative vector sum of the transverse momenta of all PF candidates in an event, and its magnitude is denoted as p_T^{miss} [107]. The $\vec{p}_T^{\,miss}$ is modified to account for corrections to the energy scale of the reconstructed jets in the event. The scalar p_T sum of all selected leptons and τ_h objects in an event is denoted as L_T, while the corresponding sum over all selected jets is designated as H_T. In addition, we define S_T as the scalar sum of p_T^{miss}, L_T, and H_T in the event. The transverse mass of charged Higgs boson candidates is calculated as:

$$m_T = \sqrt{(E_T^1 + E_T^2 + E_T^W + p_T^{miss})^2 - |\vec{p}_T^{\,1} + \vec{p}_T^{\,2} + \vec{p}_T^{\,W} + \vec{p}_T^{\,miss}|^2}, \quad (1)$$

where E_T^1, E_T^2, and E_T^W are the total visible transverse energies of the two tau lepton and W boson decay products, respectively, and $\vec{p}_T^{\,1}$, $\vec{p}_T^{\,2}$, and $\vec{p}_T^{\,W}$ the corresponding transverse momentum vectors.

Hadronic decays of top quarks are reconstructed and identified using a resolved top quark (t^{res}) tagger that is based on a fully connected neural network implemented using KERAS [108] and TENSORFLOW [109] software packages. It targets top quarks whose decay products are resolved as three separate anti-k_T jets with a distance parameter of 0.4. It is trained on simulated $t\bar{t}$ events to discriminate between three-jet combinations originating from the decay of top quarks (signal) and other combinatorial three-jet systems (background). For training, the signal t^{res} candidates are matched to the generated top quark decay products with one-to-one jet-to-quark matching, while the t^{res} candidates with at least one unmatched jet are considered as combinatorial background.

This MVA classifier utilizes high-level information from each of the three seed jets, such as invariant masses, angular separations, jet flavor, and jet shape variables. All the selected variables are uncorrelated with the top quark mass to minimize possible correlations between the t^{res} candidate mass and the associated classifier output. To improve the stability and performance of the learning algorithm, the input features are transformed such that they are distributed in similar ranges and not influenced by outliers. This tagger uses the robust scaler preprocessing method via SCIKIT-LEARN tool [110]. Furthermore to prevent mass sculpting effects, the algorithm uses the sample-reweighting technique to decorrelate the classifier's output from the top quark mass. The mass information is removed from all the input features by reweighting the combinatorial background data sets so that the t^{res} candidate mass distribution matches that of the signal.

The performance of the t^{res} tagger is expressed as a receiver operating characteristic curve and it is shown in Fig. 3. The loose, medium, and tight working points are established at 10, 5, and 1% background misidentification probability. The corresponding identification efficiencies are 91, 81, and 47%, respectively. The loose working point is employed in this analysis.

The misidentification rate and tagging efficiency of the t^{res} tagger have been estimated and compared in data and simulation to extract data-to-simulation corrections, using a sample of

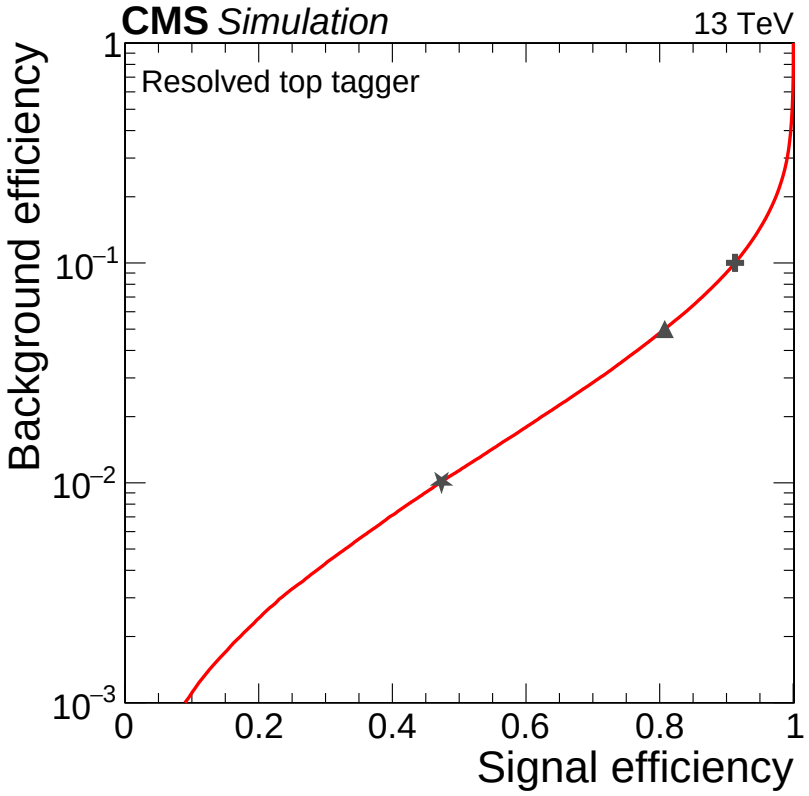

Figure 3: Receiver operating characteristic curve of the t^{res} tagger. The cross-, triangle-, and star-shaped markers indicate the loose, medium, and tight working points with 10, 5, and 1% background misidentification probability. The corresponding identification efficiencies are 91, 81, and 47%, respectively.

lepton+jets, dominated by the semileptonic $t\bar{t}$ events. The events are characterized by large p_T^{miss}, exactly one muon identified as tight with $p_T > 50\,GeV$ and at least four jets with $p_T > 40\,GeV$ and $|\eta| < 2.4$, of which at least one is b tagged. The jet closest to the muon is considered as the b jet from the leptonic top quark decay. The three-jet system with a mass closest to the top quark mass is selected as the hadronic t^{res} candidate. The misidentification rate is measured using events in which the t^{res} candidate mass, $m_{t^{res}}$, falls outside a mass window of 130–210 GeV, and the sample is dominated by the combinatorial background. Events where $m_{t^{res}}$ is within the mass window are used to measure the t^{res} tagging efficiency, after subtracting from data the contributions from non-top quark processes and the combinatorial background, as estimated from simulations. The misidentification rate and tagging efficiency for the 2017 data set are shown in Fig. 4 as a function of the t^{res} candidate p_T for the loose working point. The data-to-simulation corrections are defined as the ratio data/simulation, in p_T bins of the t^{res} candidate. Similar behavior was also observed for the 2016 and 2018 data.

5 Event selection

The analysis is conducted in the mutually exclusive $e\tau_h$, $\mu\tau_h$, $e\tau_h\tau_h$, and $\mu\tau_h\tau_h$ final states. The event selection strategy is independently optimized for each final state to improve the suppression of backgrounds while maintaining a large signal selection efficiency. The selection of signal candidate events at the trigger level is based on the presence of at least a single isolated lepton. More specifically, for the $e\tau_h$ and $e\tau_h\tau_h$ channels the online HLT requires the presence

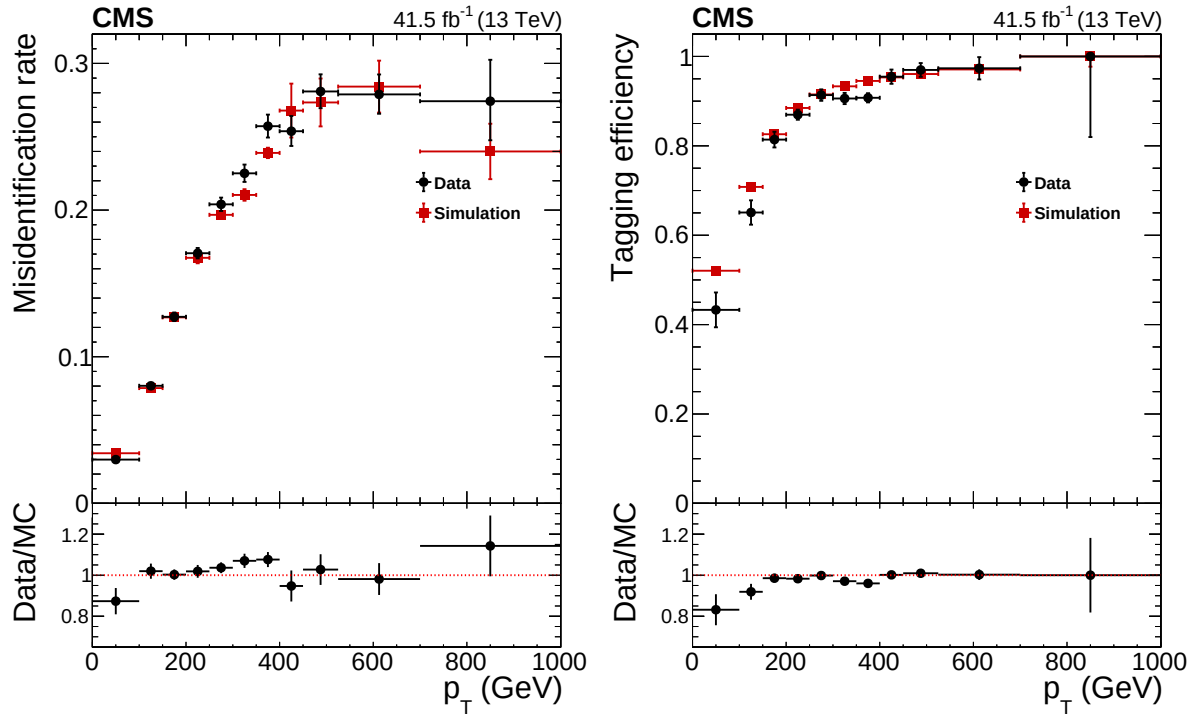

Figure 4: Misidentification rate (left) and t^{res}-tagging efficiency (right) in data and simulation, as a function of the t^{res} candidate p_T for the loose working point, using the 2017 data.

of an isolated electron with a p_T threshold of 27, 32, and 32 GeV for the data-taking years 2016, 2017, and 2018, respectively. For the $\mu\tau_h$ and $\mu\tau_h\tau_h$ channels, an isolated muon is required, with p_T thresholds of 24, 27, and 24 GeV for the three years. The HLT objects are geometrically matched to analogous offline objects that satisfy the p_T, η, I_{rel} criteria described in the following, in addition to the object identification requirements given in Section 4.

To ensure high trigger efficiency, the offline p_T and η requirements for prompt electrons (muons) are $p_T > 30$, 35, 35 (26, 29, 26) GeV and $|\eta| \leq 2.1$ (2.4) for the 2016, 2017, and 2018 data-taking periods. Selected electrons (muons) are also required to pass medium (tight) identification criteria and satisfy $I_{rel} < 0.15$ for all three years. Only events with exactly one such electron (muon) are accepted. Furthermore, events with any additional electrons or muons fulfilling looser identification criteria are also discarded, provided that the electron (muon) candidates satisfy the requirements of $p_T > 10$ GeV, $|\eta| \leq 2.4$ (2.5), and $I_{rel} < 0.25$. This helps to avoid the incorrect assignment of objects in the transverse mass reconstruction and the inadvertent smearing of its Jacobian peak, and ensures the orthogonality between final states with different lepton flavors.

In both the $\ell\tau_h$ and $\ell\tau_h\tau_h$ final states, all τ_h candidates are required to have $p_T > 20$ GeV and $|\eta| < 2.3$. They must be well separated in η-ϕ space from the trigger lepton and other τ_h candidates, such that $\Delta R(\tau_h, \ell/\tau_h) > 0.5$. To reduce the contribution of electrons, muons, or jets mimicking a τ_h object, the medium, tight, and medium working points of the D_e, D_μ, and D_j discriminants are chosen, irrespective of final state, or year of data taking. In the $\ell\tau_h$ final states, the events are classified according to the sum of the electric charge of the selected lepton and τ_h objects, $Q_{\ell\tau_h}$, in units of the electron charge e. Both the opposite-sign (OS) case with $|Q_{\ell\tau_h}| = 0$ and the same-sign (SS) case with $|Q_{\ell\tau_h}| = 2$ are considered as separate categories. The categorisation of the $\ell\tau_h$ final states into OS and SS significantly improves the expected sensitivity over the entire $m_{H^\pm}$ region considered. Events in the $\ell\tau_h$ SS category arise when one

of the tau leptons from the $H \to \tau\tau$ decay is not reconstructed or identified. It has significantly smaller contributions from SM processes with a top quark in the final state than the $\ell\tau_h$ OS category. In the $\ell\tau_h\tau_h$ final states, the two τ_h candidates are required to be OS with $|Q_{\tau_h\tau_h}| = 0$.

The $\ell\tau_h$ final states are required to contain at least three jets with $p_T > 30\,\text{GeV}$ and $|\eta| < 2.4$, for all data-taking years. Slightly modified criteria are used for the $\ell\tau_h\tau_h$ final states, with the multiplicity requirement reduced to two and the pseudorapidity extended to $|\eta| < 4.7$, in order to increase the signal acceptance. All selected jets must be well separated from the reconstructed τ_h objects such that $\Delta R(j, \tau_h) > 0.5$. We denote the selected jet with the highest (second-highest) p_T in each event as j_1 (j_2). For all final states considered, at least one of the selected jets is required to pass the medium working point of the DEEPJETb jet identification algorithm.

To further suppress multijet events with nonprompt leptons and jets misidentified as τ_h, the $\ell\tau_h$ ($\ell\tau_h\tau_h$) final states require the presence of moderate magnitude of missing transverse momentum of $p_T^{\text{miss}} \geq 40$ (30) GeV. For the $\ell\tau_h\tau_h$ final state, the requirement $S_T > 400\,\text{GeV}$ is also used as it considerably improves the expected sensitivity. A summary of the event selection criteria for all final states is shown in Table 1. They result in a total of 6 signal regions (SRs) per year of data taking; eτ_h OS, eτ_h SS, $\mu\tau_h$ OS, $\mu\tau_h$ SS, e$\tau_h\tau_h$, and $\mu\tau_h\tau_h$. They are complemented by the various control regions (CRs) and validation regions (VRs) described in Section 6, which are used to predict the dominant backgrounds in the statistical inference of the signal.

6 Background estimation

The dominant background for all the final states considered stems from V+jets and $t\bar{t}$ productions. This can be decomposed into events with genuine τ_h candidates, and events with leptons or jets misidentified as τ_h candidates. Backgrounds from events with genuine τ_h candidates, together with events involving electrons or muons misidentified as τ_h objects ($\ell \to \tau_h$) are estimated from simulation. The reconstructed τ_h candidate is matched to a generator-level tau lepton, electron, or muon using a cone of $\Delta R = 0.1$. Backgrounds from jets misidentified as τ_h candidates ($j \to \tau_h$) are estimated using control samples in data by the use of misidentification rates. These misidentification rates are measured in dedicated CRs that are enriched in jets misidentified as τ_h candidates, and mimic as closely as possible the composition and kinematic properties of the corresponding SRs. The CRs are required to be orthogonal to all SRs and have negligible signal contamination. Then, the misidentification rate is defined as:

$$\mathcal{R}_{j\to\tau_h} = \frac{N^{\text{CR}}_{\text{nominal }\tau_h}}{N^{\text{CR}}_{\text{loose},\tau_h}} \tag{2}$$

where $N^{\text{CR}}_{\text{nominal }\tau_h}$ is the number of events in the CR satisfying the nominal τ_h selection criteria, and $N^{\text{CR}}_{\text{loose }\tau_h}$ is the corresponding number of events in the CR satisfying loose τ_h selection criteria. For both the numerator and denominator in Eq. (2) a correction is applied to remove events containing jets originating from a genuine τ_h candidate or from a lepton misidentified as a τ_h candidate.

The misidentification rate measurements are performed in different CRs, separately for each final state and data-taking period. In the $\ell\tau_h$ channels, the CRs are selected with the nominal criteria used in defining the SRs, but with the following modifications. The p_T^{miss} criterion is inverted such that $p_T^{\text{miss}} < 40\,\text{GeV}$, while the requirement of exactly one t^{res} object is also in-

Table 1: Offline selections applied to the reconstructed objects to obtain the SRs of the $\ell\tau_h$ and $\ell\tau_h\tau_h$ final states. The p_T, p_T^{miss}, and S_T variables are reported in units of GeV, and Q in units of e. Selection criteria that depend on the year of data taking are presented in parentheses with the order corresponding to (2016, 2017, 2018). The symbol $\star$ is used to represent an electron (muon) for the $e\tau_h$ ($\mu\tau_h$) final states, and a τ_h object in the $e\tau_h\tau_h$ and $\mu\tau_h\tau_h$ final states.

Object	Selection	Signal Regions			
		$e\tau_h$	$\mu\tau_h$	$e\tau_h\tau_h$	$\mu\tau_h\tau_h$
Prompt electrons	N	$=1$	$=0$	$=1$	$=0$
	p_T	$>(30, 35, 35)$	>10	$>(30, 35, 35)$	>10
	$\lvert\eta\rvert$	<2.1	<2.5	<2.1	<2.5
	I_{rel}	<0.15	<0.25	<0.15	<0.25
Prompt muons	N	$=0$	$=1$	$=0$	$=1$
	p_T	>10	$>(26, 29, 26)$	>10	$>(26, 29, 26)$
	$\lvert\eta\rvert$	<2.4	<2.4	<2.4	<2.4
	I_{rel}	<0.25	<0.15	<0.25	<0.15
τ_h objects	N	$=1$		$=2$	
	p_T	>20		>20	
	$\lvert\eta\rvert$	<2.3		<2.3	
	$\lvert Q_{\star\tau_h}\rvert$	$=0, 2$		$=0$	
Jets	N	≥ 3		≥ 2	
	p_T	>30		>30	
	$\lvert\eta\rvert$	<2.4		<4.7	
b jets	N	≥ 1		≥ 1	
	p_T	>30		>30	
	$\lvert\eta\rvert$	<2.4		<2.4	
Event-based	p_T^{miss}	>40		>30	
	S_T	—		>400	

troduced to suppress contributions from V+jets processes. The motivation for these selections is twofold: to enforce orthogonality with the SRs, and to ensure that the obtained regions are enriched in $t\bar{t}$. A second set of CRs, orthogonal to all other CRs and SRs, is also used with alternative selection criteria that are introduced to enhance electroweak contributions. More specifically, the p_T^{miss} requirement is removed, the b jet multiplicity is inverted, and the requirement of exactly one t^{res} object is also imposed. These auxiliary CRs are used to quantify systematic uncertainties related to differences in sample composition between the SRs and the CRs, and in particular the relative contribution of $t\bar{t}$ and electroweak processes. The misidentification rates are measured as a function of the τ_h candidate p_T, separately for one- and three-prong decays, and individually for the central ($|\eta| \leq 1.5$) and forward regions ($|\eta| \geq 1.5$) of the detector.

In the $\ell\tau_h\tau_h$ channels, the misidentification rates are measured using similar event selection as in the SRs, except that the two τ_h objects are required to be SS with $|Q_{\tau_h\tau_h}| = 2$, and no requirement is imposed on the S_T variable. To compensate for the lower statistical precision relative to the $\ell\tau_h$ final states, the misidentification rates are parametrized in the p_T and decay mode of the τ_h objects, without separating the central and forward regions of the detector.

The predicted number of events with misidentified τ_{h} objects in the SRs is derived using the fake factor method [111] by applying the misidentification rates evaluated in the CRs to events with anti-isolated τ_{h} objects:

$$N^{\mathrm{SR}}_{j\to\tau_{\mathrm{h}}} = \sum_i w_i^{\mathrm{CR}} N^{\mathrm{SR}}_{\text{one anti-isolated } \tau_{\mathrm{h}},i} - \sum_i w^{\mathrm{CR}}_{i,\,1} w^{\mathrm{CR}}_{i,\,2} N^{\mathrm{SR}}_{\text{two anti-isolated}\tau_{\mathrm{h}},i}. \tag{3}$$

The index i refers to each bin of the parametrization and w_i to the corresponding normalization weight. The term $N^{\mathrm{SR}}_{\text{anti-isolated } \tau_{\mathrm{h}},i}$ refers to number of events with anti-isolated τ_{h} objects in the SR of interest, after subtracting events with jets originating from a genuine τ_{h} or from a lepton misidentified as a τ_{h} candidate. The normalization weight for a given parametrization bin i is given by:

$$w_i^{\mathrm{CR}} = \frac{\mathcal{R}_{j\to\tau_{\mathrm{h}},\,i}}{1-\mathcal{R}_{j\to\tau_{\mathrm{h}},\,i}} \tag{4}$$

for each event with a single anti-isolated τ_{h} candidate present. In the $\ell\tau_{\mathrm{h}}\tau_{\mathrm{h}}$ final states, Eq. (4) must be applied to each of the two τ_{h} candidates that are present. It thus accounts for the case where only one of the τ_{h} candidate is a misidentified τ_{h}, but also includes cases whereby both τ_{h} candidates are misidentified and one of them passes all nominal identification criteria. In order to account for this double counting, the number of misidentified τ_{h} events is predicted by the weighted sum of the number of events with one anti-isolated τ_{h} candidate minus the weighted number of events with two anti-isolated τ_{h} candidates.

The validity of the extracted misidentification rates is verified by defining additional VRs with either anti-isolated or isolated τ_{h} candidates, mutually orthogonal to both the SRs and CRs. The misidentification rates are used to normalize the misidentified τ_{h} samples from the anti-isolated VRs to a signal-depleted VR with isolated τ_{h} candidates, where the obtained background prediction is compared with the observed data. This validation is performed separately for all channels and data-taking periods.

In the $\ell\tau_{\mathrm{h}}$ channels, the VRs are defined by selecting events with the same selection criteria as those used for the SRs. However, instead of requiring the presence of one b jet in the $\mathrm{e}\tau_{\mathrm{h}}$ ($\mu\tau_{\mathrm{h}}$) region, a low-p_{T} loosely identified and loosely isolated displaced muon (electron) is required. In the $\ell\tau_{\mathrm{h}}\tau_{\mathrm{h}}$ channels, the validation of the background estimation is performed using two VRs. The first VR is defined by using similar event selections to the SRs but vetoing events with identified b jets, while also removing any requirements on the S_{T} variable. For the second VR, events are selected with identical criteria as for the SR, except that the S_{T} requirement is inverted to satisfy $S_{\mathrm{T}} < 400\,\mathrm{GeV}$. A summary of the event selection criteria for the CRs and the VRs used is shown in Table 2, indicating only selections that are different than their respective SRs defined in Table 1.

7 Search strategy

To maximize the sensitivity of the search, the discriminating variable used to separate between the signal and background processes is chosen separately for the $\ell\tau_{\mathrm{h}}$ and $\ell\tau_{\mathrm{h}}\tau_{\mathrm{h}}$ final states. For the latter, the search strategy focuses on the reconstruction of the full $\mathrm{H}^{\pm}$ decay chain in order to search for localized excesses in the m_{T} spectrum, as per Eq. (1). For the hypothetical signal, the m_{T} distribution should possess a Jacobian peak with an endpoint at $m_{\mathrm{T}} = m_{\mathrm{H}^{\pm}}$ that remains unchanged by the transverse motion of the mother particle. For the $\ell\tau_{\mathrm{h}}$ final states, the ambiguity in the selection of the jets that go into the m_{T} calculation results in a combinatorial background that smears the discriminating power of the variable. Thus, while still valuable, the m_{T} is not an optimal variable for signal extraction in the $\ell\tau_{\mathrm{h}}$ channels.

Table 2: Offline selections applied to the reconstructed objects to obtain the CRs and VRs for the misidentified τ_h candidate background estimation in the $\ell\tau_h$ and $\ell\tau_h\tau_h$ final states. Only differences with respect to the corresponding SRs are shown. The p_T, p_T^{miss}, and S_T variables are reported in units of GeV, and Q in units of e. The symbol $\star$ is used to represent an electron (muon) for the $e\tau_h$ ($\mu\tau_h$) final states, and a τ_h object in the $e\tau_h\tau_h$ and $\mu\tau_h\tau_h$ final states.

Object	Selection	Control Regions		Validation Regions			
		$\ell\tau_h$	$\ell\tau_h\tau_h$	$e\tau_h$	$\mu\tau_h$	$\ell\tau_h\tau_h$	
Displaced electrons	N	—	—	—	=1	—	—
	p_T	—	—	—	>10	—	—
	$\lvert\eta\rvert$	—	—	—	<2.5	—	—
	I_{rel}	—	—	—	<0.25	—	—
Displaced muons	N	—	—	=1	—	—	—
	p_T	—	—	>10	—	—	—
	$\lvert\eta\rvert$	—	—	<2.4	—	—	—
	I_{rel}	—	—	<0.25	—	—	—
τ_h objects	$\lvert Q_{\star\tau_h}\rvert$	—	=2	—	—	—	—
b jets	N	—	—	≥0	≥0	=0	—
t^{res}	N	=1	—	—	—	—	—
Event-based	p_T^{miss}	<40	—	—	—	—	—
	S_T	—	>0	—	—	>0	< 400

In order to enhance the signal and background separation in the $\ell\tau_h$ final states, an MVA BDTG classifier is employed using the TMVA [112] framework. The training was performed separately for each simulated signal sample, final state, and data-taking period. The inclusive V+jets and $t\bar{t}$ simulated samples were used to train against the background, weighted according to their cross-sections. A total of 12 input variables were used for the training of the BDTG classifiers and include kinematic variables of individual physics objects, as well as event-based variables. They are summarized in Table 3.

Three of these variables are shown in Fig. 5 for the $\mu\tau_h$ final state and the 2018 data-taking period. Figure 5 (top left) shows the azimuthal angle between the μ and $\vec{p}_T^{miss}$, denoted as $\Delta\phi(\mu, \vec{p}_T^{miss})$. In the same figure (top right) the ratio of the p_T of the third leading jet and the H_T, denoted as $p_T^{j_3}/H_T$ is shown. Finally, the transverse mass $m_T(\mu, \tau_h, j_1, j_2, \vec{p}_T^{miss})$ reconstructed from the selected μ, τ_h, j_1, j_2, and $\vec{p}_T^{miss}$ objects is shown in Fig. 5 (bottom). Instead of being used as an input to the BDTG, the event-variable $Q_{\ell\tau_h}$ is used for the categorization of $\ell\tau_h$ events, as it increases signal sensitivity over the entire mass spectrum. In particular, the SS selection significantly suppresses the $t\bar{t}$ contribution that dominates the OS category, leaving the misidentified τ_h as the dominant background.

8 Systematic uncertainties

The systematic uncertainties from various experimental and theoretical sources can affect the expected event yield (rate uncertainties), the shape of the fit discriminant (shape uncertainties), or both. Log-normal (Gaussian) a priori distributions are assumed for rate (shape) uncertain-

Table 3: The complete set of discriminating variables used in the training of the BDTG classifier employed in the search strategy of the $\ell\tau_h$ final states.

Variable	Description
$\Delta\phi(\tau_h, \vec{p}_T^{\,miss})$	azimuthal angle between the τ_h and $\vec{p}_T^{\,miss}$ objects
$\Delta\phi(\ell, \vec{p}_T^{\,miss})$	azimuthal angle between the ℓ and $\vec{p}_T^{\,miss}$ objects
$\frac{p_T^{j_1 j_2} - p_T^{H^\pm}}{p_T^{j_1 j_2} + p_T^{H^\pm}}$	ratio of p_T sums calculated from ℓ, τ_h, j_1, j_2 and $\vec{p}_T^{\,miss}$
$\frac{p_T^{j_1 j_2}}{H_T}$	ratio of p_T of the first two leading jets and the H_T
$m_T(\ell, \tau_h, j_1, j_2, \vec{p}_T^{\,miss})$	m_T reconstructed from ℓ, τ_h, j_1, j_2, and $\vec{p}_T^{\,miss}$
$\frac{p_T^{j_3}}{H_T}$	ratio of the p_T of the third leading jet and the H_T
$m(\ell, \tau_h)$	invariant mass of the ℓ and τ_h objects
$\frac{p_T^{j_1 j_2} + L_T}{H_T}$	ratio of p_T of first two leading jets plus L_T and the H_T
$m_T(\ell, \vec{p}_T^{\,miss})$	m_T reconstructed from the ℓ and $\vec{p}_T^{\,miss}$ objects
$p_T^{\tau_h}$	transverse momentum of τ_h object
N_{jets}	number of selected jets in the event
$N_{t^{res}}$	number of selected t^{res} objects in the event

ties. Partial and complete correlations between the uncertainties in different categories and years are taken into account, depending on the way they are derived. All experimental sources are treated as correlated across categories but as uncorrelated across years, unless otherwise specified. All theoretical sources are treated as correlated across all categories and years. A summary of all sources of systematic uncertainties discussed in this section is given in Table 4.

Apart from the various experimental uncertainties, the statistical analysis of the results employs an uncertainty model that also accounts for uncertainties due to the limited population of template distributions in signal and background modeling. These statistical uncertainties can lead to fluctuations in nominal predictions and their effect is individually incorporated for each template bin with the *Barlow–Beeston lite* approach [113, 114]. Each bin is assigned a combined statistical uncertainty, and these uncertainties are treated as uncorrelated among other bins, categories, channels, and data sets.

8.1 Experimental sources

The integrated luminosity for each year of data taking is measured individually with an uncertainty in the 1.2–2.5% range [115–117]. The total integrated luminosity for the period 2016–2018 has an uncertainty of 1.6%. The improvement in precision reflects the uncorrelated time evolution of some systematic effects. These effects are applied as rate uncertainties to all simulated processes and thus only affect the expected yield of events, but not the individual shapes of the fit discriminants.

Uncertainties related to the electron and muon trigger efficiencies arise from the fact that sim-

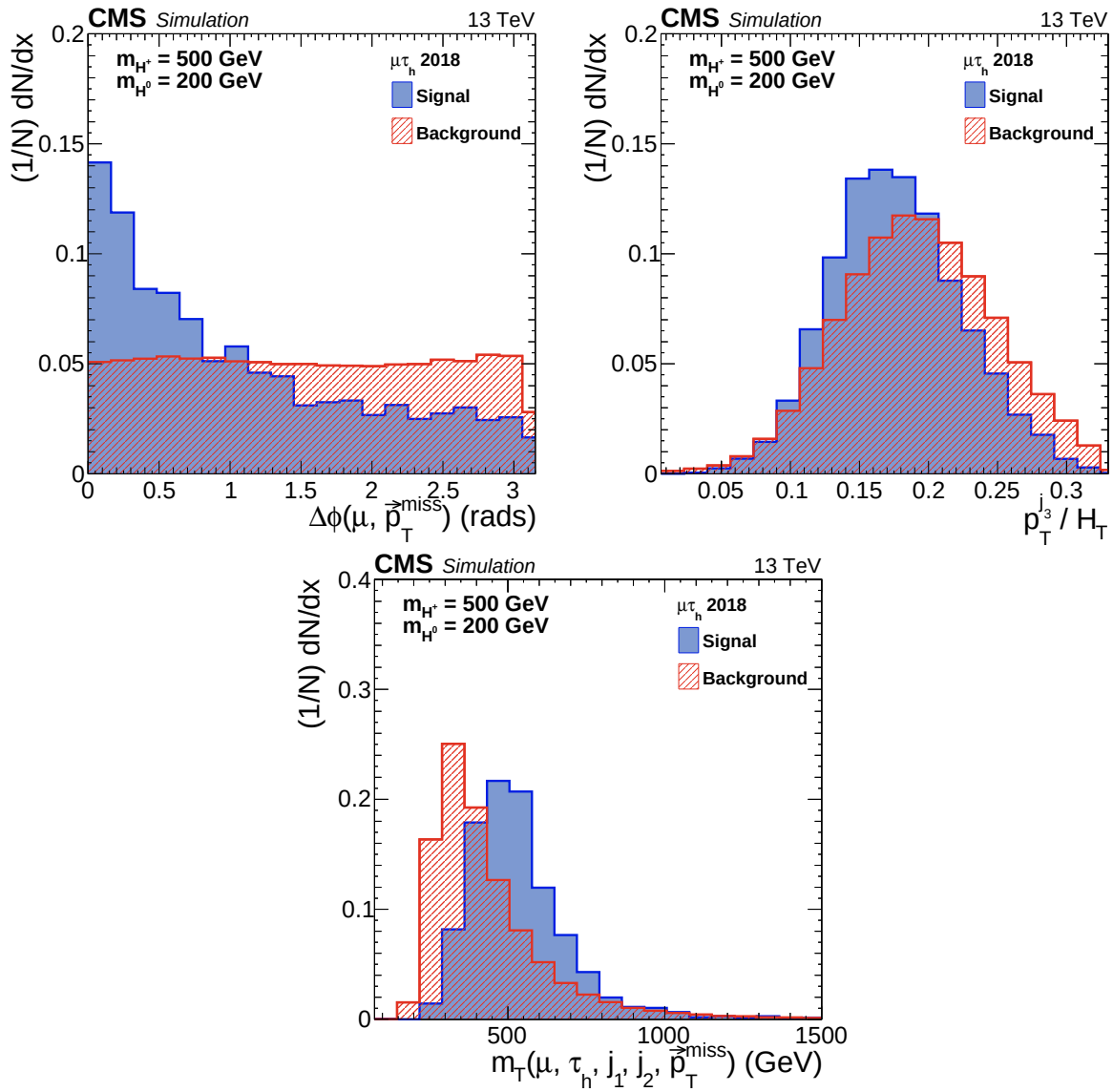

Figure 5: Three of the BDTG input variables used for the $\mu\tau_h$ final state, assuming a signal with mass $m_{H^\pm} = 500$ GeVand 2018 data-taking conditions: the azimuthal angle between the μ and $\vec{p}_T^{miss}$ objects (top left), the ratio of the p_T of the third leading jet and the H_T (top right), and the transverse mass reconstructed from the μ, τ_h, j_1, j_2, and $\vec{p}_T^{miss}$ objects (bottom). Both signal and background distributions are normalized to unit area.

ulated events are corrected to match the efficiencies measured in data. The uncertainties in the corrections, which depend on the p_T and η of the trigger object, lead to rate and shape effects in the fit discriminants that amount to 1–4%.

During the 2016–2017 data taking, a gradual shift in the timing of the ECAL inputs to the first-level trigger in the region of $|\eta| > 2.0$ caused a trigger inefficiency of ≈10–20% for events containing an electron (jet) with $p_T \gtrsim 50$ (100) GeV and in the region $2.5 < |\eta| < 3.0$, depending on p_T, η, and time. Corresponding correction factors were derived from data and applied to the acceptance evaluated from simulation. The related uncertainties, which are treated as correlated between the two years and all categories, are found to affect the expected event yields by ≈1% when propagated to the final fit discriminants.

The uncertainty due to the pileup modeling in simulated samples is estimated by varying the total inelastic pp cross section used to estimate the number of pileup events in data. The nominal value of 69.2 mb is varied by 5% [118, 119] and the effect is propagated through all event selections. The resulting uncertainty amounts to up to 5.5%, and is treated as correlated across all categories and years.

Uncertainties associated with the identification efficiency for electrons and muons are propagated as variations to the final fit discriminants. They are treated as correlated across all categories and years and result in shape-altering variations that change the total event yield by about 0.1–2.4%. The uncertainty related to the vetoing of leptons passing loose selection criteria is between 0.1 and 2.0%.

The uncertainties associated with the τ_h identification efficiency are evaluated in p_T bins of the τ_h object and range between 0.1 and 5.3%. The τ_h energy scale uncertainties are found to be up to about 2.0%, depending on the decay mode of the τ_h object. For the energy and momentum scale of electrons and muons misidentified as τ_h candidates, the relevant corrections depend on the p_T and decay mode of the candidate and their uncertainties are of $\mathcal{O}(1\%)$. The above-mentioned uncertainties lead to shape effects and are treated as uncorrelated across p_T bins and decay modes.

The jet energy scale uncertainties are specified as functions of jet p_T and η and are treated as correlated across all categories and years. They are estimated by shifting the energy of jets and propagating these shifts through the analysis selections. This results in rate- and shape-altering variations of $\mathcal{O}(5\%)$. The energy resolution of simulated jets is adjusted to match the resolution observed in data. The uncertainties in the jet energy resolution are evaluated by smearing the jet energies around their nominal values. These are treated as uncorrelated across the years and correlated across categories and result in an overall effect of $\mathcal{O}(5\%)$.

Jet energy uncertainties are also propagated to the $\vec{p}_T^{\,miss}$ calculation to account for the fact that it primarily relies on the accurate measurement of the reconstructed physics objects. Another uncertainty in the $\vec{p}_T^{\,miss}$ measurement is related to the unclustered energy in the event. It refers to jets with $p_T < 10\,\text{GeV}$ and PF candidates not clustered into jets. This unclustered energy scale uncertainty impacts both the rate and the shape of the fit discriminants and has an overall effect of up to 2.4%.

The efficiency of classifying jets as b tagged is different in data than in simulation. To correct for this effect p_T-dependent corrections are incorporated. The systematic uncertainties in these tagging and mistagging efficiency corrections are treated as rate and shape altering. They are found to have an effect of $\mathcal{O}(5\%)$ in the expected event yields.

The uncertainties associated with the t^{res} tagging and mistagging efficiency corrections are only relevant for the $\ell\tau_h$ categories. They are evaluated in bins of p_T of the selected t^{res} and the various sources of uncertainty are treated as uncorrelated. These include effects due to the generator-level matching definition, the damping of radiation with high p_T, the modeling of the first emission, the scale radiation, the color reconnection strength, the assumed value of the top quark mass, and the tuning of the underlying event parameters. These are propagated to the fit discriminants of the $\ell\tau_h$ final states as shape uncertainties and are found to change the total event yield by about 5% for tagging and 8% for mistagging.

For the misidentified τ_h background estimation three distinct components of uncertainties are defined. The first component is the statistical uncertainty associated with the evaluation of the misidentification rates in the dedicated CRs. The various parametrization bins that are used in the $\ell\tau_h$ and $\ell\tau_h\tau_h$ channels for this measurement, as described in Section 6, are treated as

uncorrelated. The propagation of the statistical uncertainty in the final fit discriminants has an overall effect of $\mathcal{O}(10\%)$. The second component is concerned with a rate and shape-altering uncertainties implemented to address the level of agreement of closure tests in the VRs. Their impact on the expected event yield is $\mathcal{O}(10\%)$. The third component accounts for the difference in sample composition between the CRs in which the misidentification rates are determined, and the SRs in which they are applied. It is treated as uncorrelated between the parametrization bins and when propagated to the final fit discriminants brings about an overall effect of up to 18%.

8.2 Theoretical sources

The systematic uncertainties related to theoretical considerations mainly arise due to missing higher-order QCD corrections and uncertainties in the PDF sets. An additional source of uncertainty concerns the assumed values of the top quark mass m_t and that of the strong coupling α_S in parton showers [120]. These affect both the total and differential cross sections of the processes, yielding uncertainties on the overall normalization of the simulated processes and the acceptance of the event selection. All effects are taken into account as rate uncertainties.

For the $t\bar{t}$ and single t processes, the effect of m_t on the cross sections is evaluated by varying its nominal value of 172.5 GeV by 1.0 GeV. The effects from the renormalization and factorization (RF) scales on the acceptance and cross sections are evaluated by varying them independently by factors of one-half and two with respect to their nominal values, respectively. Extreme variations where one scale is varied by one-half and the other one by two are excluded. The effect on the event yield from simulated events is then calculated by enveloping the maximum variation with respect to the nominal fit discriminants, as recommended in Ref. [121].

The PDF uncertainties are also treated as fully correlated for all processes and categories. They are also correlated between simulated samples that share the same dominant partons in the initial state of the ME calculations [122].

9 Results

Binned MVA output distributions in the $\ell\tau_h$ analysis and m_T distributions in the $\ell\tau_h\tau_h$ analysis are used to test the compatibility of the observed data with the presence or absence of a signal. Data are split in 6 categories determined by the lepton flavor in the final state (e or μ), for each of the three years of data taking. For the $\ell\tau_h$ final states the number of categories is double due to the consideration of the sum of the electric charge of the lepton and τ_h objects. Therefore there are 18 categories in total; 12 associated with the $\ell\tau_h$ analysis and 6 with the $\ell\tau_h\tau_h$ analysis. A simultaneous binned maximum likelihood fit is performed over all categories and data sets. The likelihood incorporates all the systematic uncertainties described in Section 8 as nuisance parameters, with shape variations taken into account via continuous morphing [114].

No significant excess is found in any of the categories considered. The distributions for the fit performed under the background-only hypothesis are shown in Figs. 6 and 7 for the $\ell\tau_h$ and $\ell\tau_h\tau_h$ final states, respectively, whereby all categories for each individual final state are added into a single distribution. For the $\ell\tau_h\tau_h$ final states, the distributions are binned with variable width and according to the statistical precision of the samples. In order to retain the shape of the distributions, each bin is divided by their width. The pre-fit contribution of a hypothetical $H^\pm \to HW^\pm$ signal with masses $m_{H^\pm} = 500$ GeVand $m_H = 200$ GeV is also shown, normalized assuming that the product of the cross section and branching fraction $\sigma_{H^\pm}\mathcal{B}(H^\pm \to HW^\pm, H \to \tau\tau)$ is 1 pb. Tabulated results are provided in the HEPData record for this analysis [123].

Table 4: Summary of all sources of systematic uncertainties discussed in the text. The first column identifies the source of uncertainty and, where applicable, the process that it applies to. The second column indicates with a check mark ✓ or dash — whether or not the nuisance parameter also affects the shape of the fit discriminant. The third column, which is subdivided into four event categories, presents the percentage % impact of these nuisance parameters on the expected event yields, before simultaneous fitting the data for the background-only hypothesis. A range of such values represents the minimum and maximum values observed through the different samples and data eras, with apparent disparities also attributed to the limited sample size of minor backgrounds. The last two columns indicate whether or not the nuisance parameters are correlated across years and categories. A dagger † designates that a nuisance parameter is only partially correlated across years or categories.

		Category				Correlated across	
Uncertainty source	Shape	$e\tau_h$	$\mu\tau_h$	$e\tau_h\tau_h$	$\mu\tau_h\tau_h$	Years	Categories
		Experimental					
Integrated luminosity	—	1.2–2.5				✓†	✓
Trigger efficiency	✓	0.9–4.2	0.5–2.9	1.2–3.0	0.1–0.3	—	✓
Trigger timing inefficiency	✓	—		0.1–0.3	0.1–0.3	—	✓
Pileup	✓	0.2–2.9	0.1–1.6	0.1–5.5	0.1–2.3	✓	✓
Electron identification	✓	0.1–2.4	—	0.1–1.9	—	✓	✓
Muon identification	✓	—	0.4–1.6	—	0.1–1.1	✓	✓
Lepton veto	—	0.1–2.0	0.1–2.0	0.1–2.0	0.1–2.0	—	✓
τ_h identification	✓	0.1–3.6	0.1–3.2	4.2–5.2	4.3–5.3	—	✓
τ_h energy scale	✓	0.2–1.8	0.2–0.4	0.8–1.5	0.8–1.2	—	✓
$e \to \tau_h$ misidentification	✓	0.2–1.5	0.1–0.4	0.3–0.6	0.2–0.6	—	✓
$\mu \to \tau_h$ misidentification	✓	0.1–1.6	0.1–0.3	0.1–0.3	0.1–0.3	—	✓
Jet energy scale	✓	1.1–4.9	1.2–4.2	1.6–3.6	1.6–2.4	✓	✓
Jet energy resolution	✓	0.3–3.1	0.3–3.1	1.1–4.6	1.2–3.1	—	✓
b jet identification	✓	2.5–5.4	2.5–5.1	2.4–4.2	3.2–4.2	—	✓
b jet misidentification	✓	2.4–4.1	2.2–4.5	1.0–2.6	1.7–2.5	—	✓
Unclustered energy scale	✓	0.1–1.9	0.2–1.5	0.5–1.7	0.3–2.4	—	✓
t^{res} tagging	✓	1.5–7.6	1.3–7.5	—	—	—	✓
t^{res} mistagging	✓	1.7–4.9	1.7–5.4	—	—	—	✓
$j \to \tau_h$ misidentification	✓	17.8–21.1	18.2–22.4	14.8	10.5	—	—
		Theoretical					
Top quark mass ($t\bar{t}$)	—	2.2				✓	✓
Top quark mass (single t)	—	2.8				✓	✓
Acceptance $H^{\pm}$ (RF scale, PDF)	—	5.3				✓	✓
Acceptance $t\bar{t}$ (RF scale, PDF)	—	-2.8 to $+2.0$				✓	✓
Acceptance single t (RF scale, PDF)	—	-2.0 to $+0.3$				✓	✓
Acceptance $t\bar{t}X$ (RF scale, PDF)	—	2.0				✓	✓
Acceptance EW (RF scale, PDF)	—	<1.0				✓	✓
Cross section $t\bar{t}$ (RF scale, PDF)	—	-4.8 to 5.5				✓	✓
Cross section single t (RF scale, PDF)	—	5.3				✓	✓
Cross section $t\bar{t}X$ (RF scale, PDF)	—	2.2				✓	✓
Cross section EW (RF scale, PDF)	—	5.4				✓	✓

The event rates, with the expected yields from the SM backgrounds normalized as resulting from a background-only fit to the data, are shown in Fig. 8, for all data sets and final states considered.

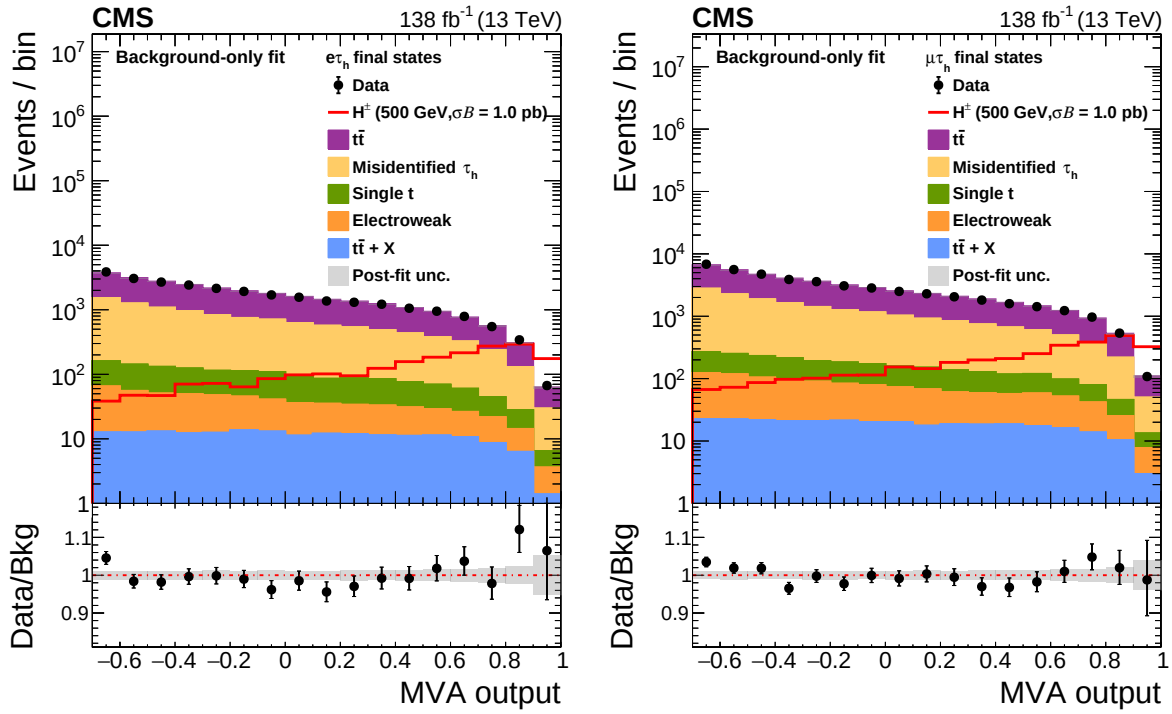

Figure 6: The MVA output of the BDTG for the $e\tau_h$ (left) and $\mu\tau_h$ (right) final states used in the limit extraction, after a background-only fit to the data. The data sets of all categories have been added. The pre-fit contribution from $H^\pm \to HW^\pm$ with masses $m_{H^\pm} = 500\,\text{GeV}$and $m_H = 200\,\text{GeV}$ and $\sigma_{H^\pm}\mathcal{B}(H^\pm \to HW^\pm, H \to \tau\tau) = 1\,\text{pb}$ is also shown.

Upper limits on $\sigma_{H^\pm}\mathcal{B}(H^\pm \to HW^\pm, H \to \tau\tau)$ for a potential $H^\pm$ signal are computed at the 95% CL, using the modified frequentist CL_s criterion [124, 125]. The definition of the profile likelihood test statistic is as defined in Ref. [126], using the asymptotic approximation [127].

The upper limit with all final states, categories, and years combined is shown in Fig. 9 (left). The observed upper limit on $\sigma_{H^\pm}\mathcal{B}(H^\pm \to HW^\pm, H \to \tau\tau)$ varies between 0.085 pb at 300 GeV to 0.019 pb at 700 GeV . In the same figure (right), the expected sensitivity from each contributing final state is also shown. The $\ell\tau_h\tau_h$ final states are the most sensitive in the whole $m_{H^\pm}$ range from 300 to 700 GeV, while the $\ell\tau_h$ final states improve the overall sensitivity by 20–35%.

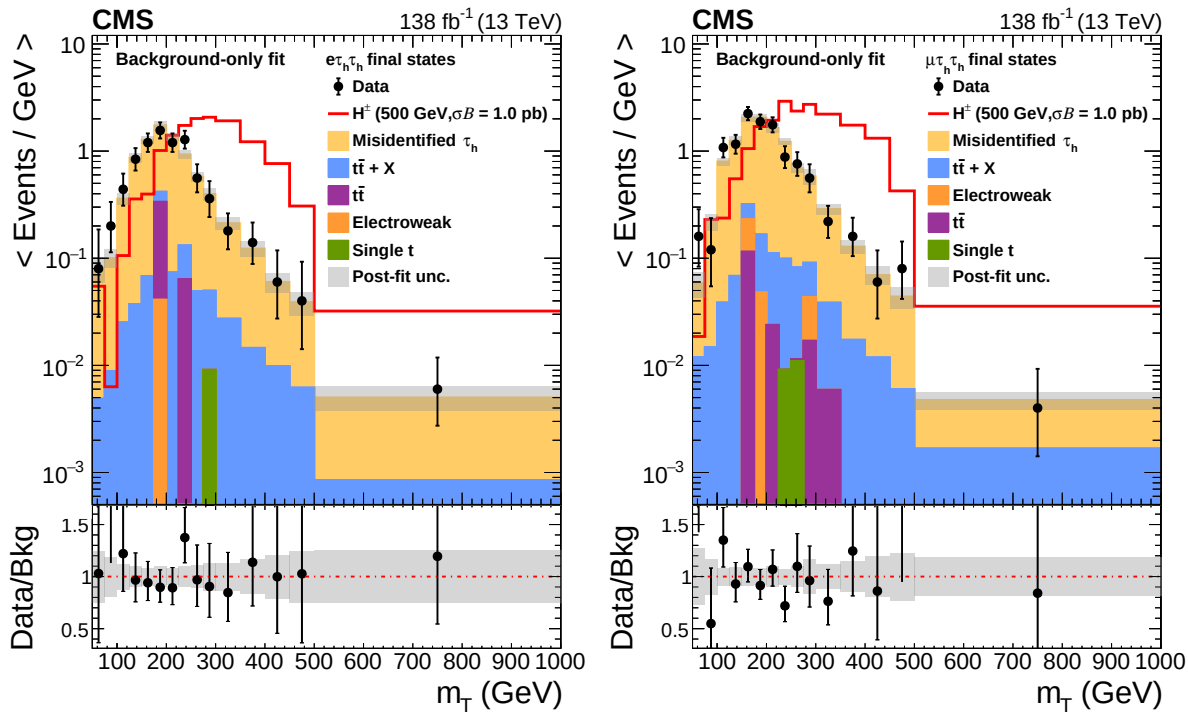

Figure 7: The m_{T} distributions for the $\mathrm{e}\tau_{\mathrm{h}}\tau_{\mathrm{h}}$ (left) and $\mu\tau_{\mathrm{h}}\tau_{\mathrm{h}}$ (right) final states used in the limit extraction, after a background-only fit to the data. The data sets of all categories have been added. The pre-fit contribution from $\mathrm{H}^{\pm} \to \mathrm{HW}^{\pm}$ with masses $m_{\mathrm{H}^{\pm}} = 500\,\mathrm{GeV}$and $m_{\mathrm{H}} = 200\,\mathrm{GeV}$ and $\sigma_{\mathrm{H}^{\pm}}\mathcal{B}(\mathrm{H}^{\pm} \to \mathrm{HW}^{\pm}, \mathrm{H} \to \tau\tau) = 1\,\mathrm{pb}$ is also shown. The brackets $\langle\cdot\rangle$ signify that the plotted variable is averaged over an interval in which the event frequency may have changed considerably.

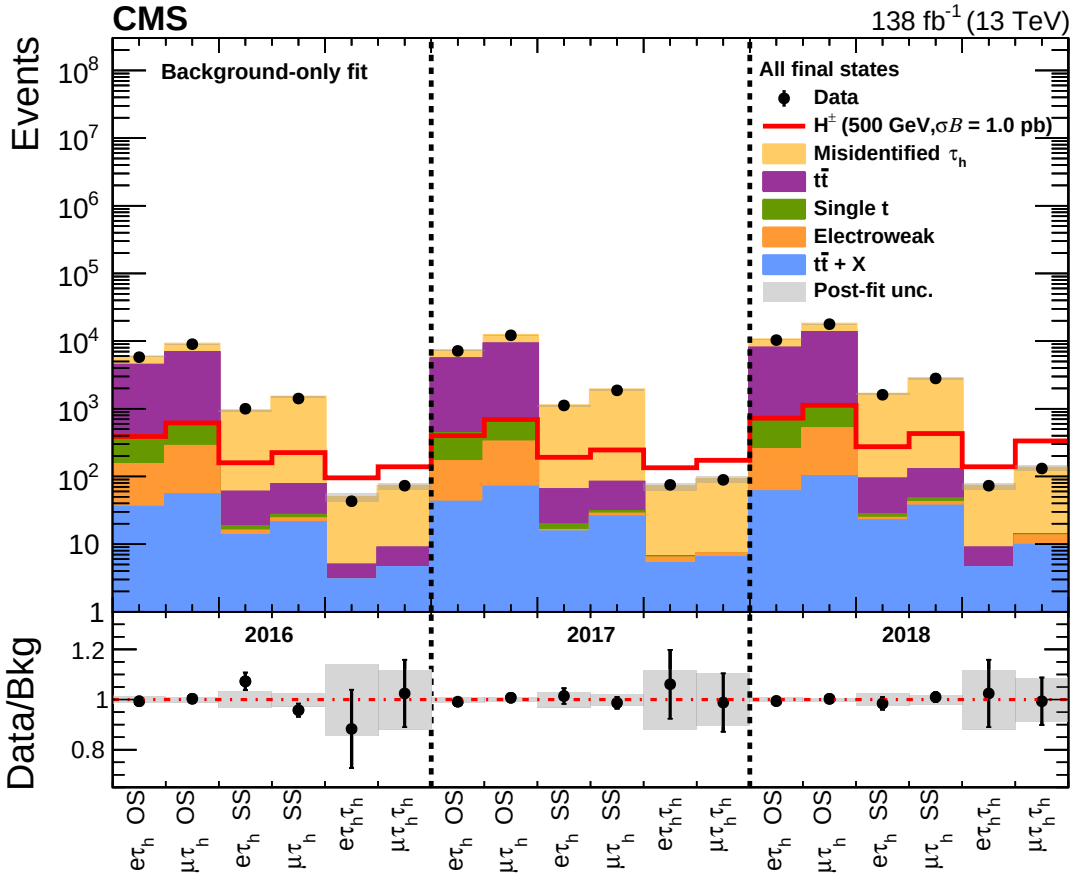

Figure 8: Observed event yields (black markers) for the 18 categories considered in this analysis, grouped into data sets that are represented by vertical dashed lines. The expected event yields (stacked histograms) resulting from a background-only fit to the data are also shown, broken down into various background processes. The solid red line represents the expected signal yields from $\mathrm{H}^{\pm} \to \mathrm{HW}^{\pm}$ with masses $m_{\mathrm{H}^{\pm}} = 500\,\mathrm{GeV}$and $m_{\mathrm{H}} = 200\,\mathrm{GeV}$, assuming $\sigma_{\mathrm{H}^{\pm}}\mathcal{B}(\mathrm{H}^{\pm} \to \mathrm{HW}^{\pm}, \mathrm{H} \to \tau\tau) = 1\,\mathrm{pb}$.

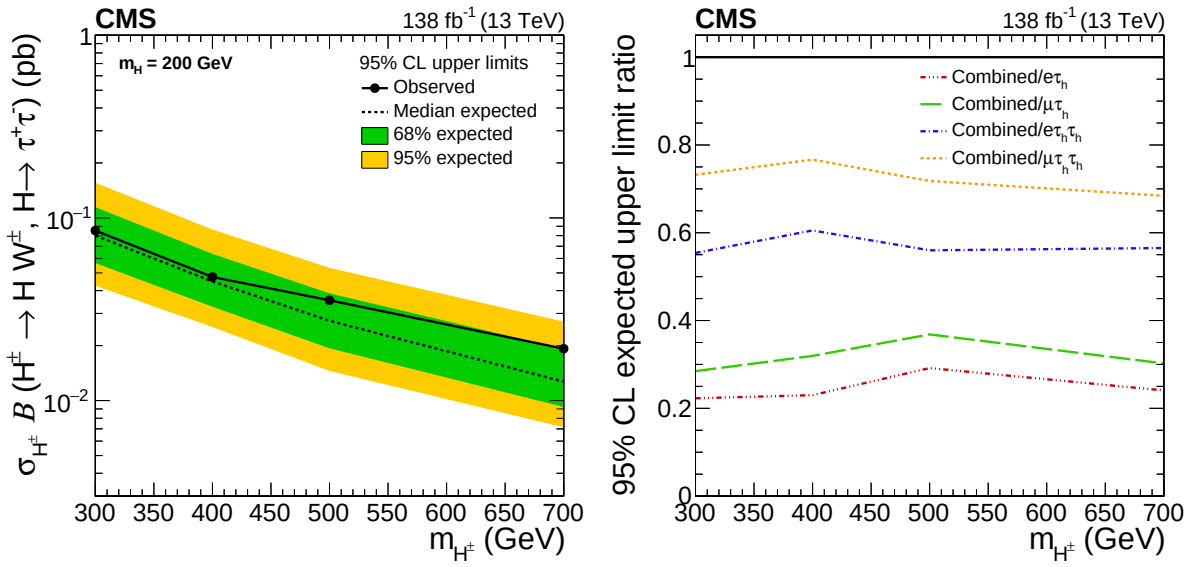

Figure 9: Expected and observed upper limits at 95% CL on the product of cross section and branching fraction $\sigma_{\mathrm{H}^{\pm}}\mathcal{B}(\mathrm{H}^{\pm} \to \mathrm{HW}^{\pm}, \mathrm{H} \to \tau\tau)$ as a function of $m_{\mathrm{H}^{\pm}}$ and assuming $m_{\mathrm{H}} = 200\,\mathrm{GeV}$ for the combination of all final states considered (left). The observed upper limits are represented by a solid black line and circle markers. The median expected limit (dashed line), 68% (inner green band), and 95% (outer yellow band) confidence intervals are also shown. The relative expected contributions of each final state to the overall combination are also presented (right). The black solid line corresponds to the combined expected limit, while the red dash-dotted, green dashed, blue dashed-dotted, and orange dashed lines represent the relative contributions from the $\mathrm{e}\tau_{\mathrm{h}}$, $\mu\tau_{\mathrm{h}}$, $\mathrm{e}\tau_{\mathrm{h}}\tau_{\mathrm{h}}$, and $\mu\tau_{\mathrm{h}}\tau_{\mathrm{h}}$ channels, respectively.

10 Summary

Results are presented from a search for a charged Higgs boson $H^{\pm}$ decaying into a heavy neutral Higgs boson H and a W boson. Events are selected with exactly one isolated electron or muon, targeting event topologies whereby the H decays into a pair of tau leptons with at least one decaying hadronically (τ_h). Four distinct final states are considered: $e\tau_h$, $\mu\tau_h$, $e\tau_h\tau_h$, and $\mu\tau_h\tau_h$. The analysis uses proton-proton collision data recorded by the CMS detector at $\sqrt{s} = 13\,\text{TeV}$, corresponding to an integrated luminosity of $138\,\text{fb}^{-1}$. No significant deviation is observed from standard model expectations. Upper limits at 95% confidence level are set on the product of the cross section and branching fraction for an $H^{\pm}$ in the mass range of 300–700 GeV, assuming an H with a mass of 200 GeV. The observed limits range from 0.085 pb for an $H^{\pm}$ mass of 300 GeV to 0.019 pb for a mass of 700 GeV. These are the first limits on $H^{\pm}$ production in the $H^{\pm} \to HW^{\pm}$ decay channel at the LHC.

References

[1] P. W. Higgs, "Broken symmetries, massless particles and gauge fields", *Phys. Lett.* **12** (1964) 132, doi:10.1016/0031-9163(64)91136-9.

[2] P. W. Higgs, "Broken symmetries and the masses of gauge bosons", *Phys. Rev. Lett.* **13** (1964) 508, doi:10.1103/PhysRevLett.13.508.

[3] G. S. Guralnik, C. R. Hagen, and T. W. B. Kibble, "Global conservation laws and massless particles", *Phys. Rev. Lett.* **13** (1964) 585, doi:10.1103/PhysRevLett.13.585.

[4] F. Englert and R. Brout, "Broken symmetry and the mass of gauge vector mesons", *Phys. Rev. Lett.* **13** (1964) 321, doi:10.1103/PhysRevLett.13.321.

[5] P. W. Higgs, "Spontaneous symmetry breakdown without massless bosons", *Phys. Rev.* **145** (1966) 1156, doi:10.1103/PhysRev.145.1156.

[6] T. W. B. Kibble, "Symmetry breaking in non-Abelian gauge theories", *Phys. Rev.* **155** (1967) 1554, doi:10.1103/PhysRev.155.1554.

[7] ATLAS Collaboration, "Observation of a new particle in the search for the standard model Higgs boson with the ATLAS detector at the LHC", *Phys. Lett. B* **716** (2012) 1, doi:10.1016/j.physletb.2012.08.020, arXiv:1207.7214.

[8] CMS Collaboration, "Observation of a new boson at a mass of 125 GeV with the CMS experiment at the LHC", *Phys. Lett. B* **716** (2012) 30, doi:10.1016/j.physletb.2012.08.021, arXiv:1207.7235.

[9] CMS Collaboration, "Observation of a new boson with mass near 125 GeV in pp collisions at $\sqrt{s} = 7$ and 8 TeV", *JHEP* **06** (2013) 081, doi:10.1007/JHEP06(2013)081, arXiv:1303.4571.

[10] ATLAS and CMS Collaborations, "Measurements of the Higgs boson production and decay rates and constraints on its couplings from a combined ATLAS and CMS analysis of the LHC pp collision data at $\sqrt{s} = 7$ and 8 TeV", *JHEP* **08** (2016) 045, doi:10.1007/JHEP08(2016)045, arXiv:1606.02266.

[11] CMS Collaboration, "Combined measurements of Higgs boson couplings in proton-proton collisions at $\sqrt{s} = 13\,\text{TeV}$", *Eur. Phys. J. C* **79** (2019) 421, doi:10.1140/epjc/s10052-019-6909-y, arXiv:1809.10733.

[12] ATLAS Collaboration, "Combined measurements of Higgs boson production and decay using up to 80 fb^{-1} of proton-proton collision data at $\sqrt{s} = 13$ TeV collected with the ATLAS experiment", *Phys. Rev. D* **101** (2020) 012002, doi:10.1103/PhysRevD.101.012002, arXiv:1909.02845.

[13] CMS Collaboration, "Measurements of the Higgs boson width and anomalous HVV couplings from on-shell and off-shell production in the four-lepton final state", *Phys. Rev. D* **99** (2019) 112003, doi:10.1103/PhysRevD.99.112003, arXiv:1901.00174.

[14] J. F. Gunion and H. E. Haber, "The CP conserving two Higgs doublet model: the approach to the decoupling limit", *Phys. Rev. D* **67** (2003) 075019, doi:10.1103/PhysRevD.67.075019, arXiv:hep-ph/0207010.

[15] A. G. Akeroyd et al., "Prospects for charged Higgs searches at the LHC", *Eur. Phys. J. C* **77** (2017) 276, doi:10.1140/epjc/s10052-017-4829-2, arXiv:1607.01320.

[16] G. C. Branco et al., "Theory and phenomenology of two-Higgs-doublet models", *Phys. Rept.* **516** (2012) 1, doi:10.1016/j.physrep.2012.02.002, arXiv:1106.0034.

[17] N. Craig and S. Thomas, "Exclusive signals of an extended Higgs sector", *JHEP* **11** (2012) 083, doi:10.1007/JHEP11(2012)083, arXiv:1207.4835.

[18] CMS Collaboration, "A measurement of the Higgs boson mass in the diphoton decay channel", *Phys. Lett. B* **805** (2020) 135425, doi:10.1016/j.physletb.2020.135425, arXiv:2002.06398.

[19] M. Carena, I. Low, N. R. Shah, and C. E. M. Wagner, "Impersonating the standard model Higgs boson: alignment without decoupling", *JHEP* **04** (2014) 015, doi:10.1007/JHEP04(2014)015, arXiv:1310.2248.

[20] R. Harlander, M. Krämer, and M. Schumacher, "Bottom-quark associated Higgs-boson production: reconciling the four- and five-flavour scheme approach", 2011. arXiv:1112.3478.

[21] H. Bahl, T. Stefaniak, and J. Wittbrodt, "The forgotten channels: charged Higgs boson decays to a $\text{W}^{\pm}$ and a non-SM-like Higgs boson", *JHEP* **06** (2021) doi:10.1007/JHEP06(2021)183, arXiv:2103.07484.

[22] ATLAS Collaboration, "Search for charged Higgs bosons decaying via $\text{H}^{\pm} \to \tau^{\pm}\nu$ in fully hadronic final states using pp collision data at $\sqrt{s} = 8$ TeV with the ATLAS detector", *JHEP* **03** (2015) 088, doi:10.1007/JHEP03(2015)088, arXiv:1412.6663.

[23] CMS Collaboration, "Search for a charged Higgs boson in pp collisions at $\sqrt{s} = 8$ TeV", *JHEP* **11** (2015) 018, doi:10.1007/JHEP11(2015)018, arXiv:1508.07774.

[24] ATLAS Collaboration, "Search for charged Higgs bosons decaying via $\text{H}^{\pm} \to \tau^{\pm}\nu_{\tau}$ in the τ+jets and τ+lepton final states with 36 fb^{-1} of pp collision data recorded at $\sqrt{s} = 13$ TeV with the ATLAS experiment", *JHEP* **09** (2018) 139, doi:10.1007/JHEP09(2018)139, arXiv:1807.07915.

[25] CMS Collaboration, "Search for charged Higgs bosons in the $\text{H}^{\pm} \to \tau^{\pm}\nu_{\tau}$ decay channel in proton-proton collisions at $\sqrt{s} = 13$ TeV", *JHEP* **07** (2019) 142, doi:10.1007/JHEP07(2019)142, arXiv:1903.04560.

[26] CMS Collaboration, "Search for a light charged Higgs boson decaying to $c\bar{s}$ in pp collisions at $\sqrt{s} = 8$ TeV", *JHEP* **12** (2015) 178, doi:10.1007/JHEP12(2015)178, arXiv:1510.04252.

[27] ATLAS Collaboration, "Search for a light charged Higgs boson in the decay channel $H^+ \to c\bar{s}$ in $t\bar{t}$ events using pp collisions at $\sqrt{s} = 7$ TeV with the ATLAS detector", *Eur. Phys. J. C* **73** (2013) 2465, doi:10.1140/epjc/s10052-013-2465-z, arXiv:1302.3694.

[28] CMS Collaboration, "Search for a charged Higgs boson decaying to charm and bottom quarks in proton-proton collisions at $\sqrt{s} = 8$ TeV", *JHEP* **11** (2018) 115, doi:10.1007/JHEP11(2018)115, arXiv:1808.06575.

[29] CMS Collaboration, "Search for a light charged Higgs boson decaying to a W boson and a CP-odd Higgs boson in final states with $e\mu\mu$ or $\mu\mu\mu$ in proton-proton collisions at $\sqrt{s} = 13$ TeV", *Phys. Rev. Lett.* **123** (2019) 131802, doi:10.1103/PhysRevLett.123.131802, arXiv:1905.07453.

[30] ATLAS Collaboration, "Search for charged Higgs bosons in the $H^\pm \to tb$ decay channel in pp collisions at $\sqrt{s} = 8$ TeV using the ATLAS detector", *JHEP* **03** (2016) 127, doi:10.1007/JHEP03(2016)127, arXiv:1512.03704.

[31] ATLAS Collaboration, "Search for charged Higgs bosons decaying into top and bottom quarks at $\sqrt{s} = 13$ TeV with the ATLAS detector", *JHEP* **11** (2018) 085, doi:10.1007/JHEP11(2018)085, arXiv:1808.03599.

[32] CMS Collaboration, "Search for a charged Higgs boson decaying into top and bottom quarks in events with electrons or muons in proton-proton collisions at $\sqrt{s} = 13$ TeV", *JHEP* **01** (2020) 096, doi:10.1007/JHEP01(2020)096, arXiv:1908.09206.

[33] ATLAS Collaboration, "Search for charged Higgs bosons produced in association with a top quark and decaying via $H^\pm \to \tau\nu$ using pp collision data recorded at $\sqrt{s} = 13$ TeV by the ATLAS detector", *Phys. Lett. B* **759** (2016) 555, doi:10.1016/j.physletb.2016.06.017, arXiv:1603.09203.

[34] CMS Collaboration, "Search for charged Higgs bosons decaying into a top and a bottom quark in the all-jet final state of pp collisions at $\sqrt{s} = 13$ TeV", *JHEP* **07** (2020) 126, doi:10.1007/JHEP07(2020)126, arXiv:2001.07763.

[35] BaBar and Belle Collaborations, "The physics of the B factories", *Eur. Phys. J. C* **74** (2014) 3026, doi:10.1140/epjc/s10052-014-3026-9, arXiv:1406.6311.

[36] Belle II Collaboration, "The Belle II Physics Book", *PTEP* **2019** (2019) 123C01, doi:10.1093/ptep/ptz106, arXiv:1808.10567. [Erratum: doi:10.1093/ptep/ptaa008].

[37] G. Senjanovic and R. N. Mohapatra, "Exact left-right symmetry and spontaneous violation of parity", *Phys. Rev. D* **12** (1975) 1502, doi:10.1103/PhysRevD.12.1502.

[38] J. F. Gunion, R. Vega, and J. Wudka, "Higgs triplets in the standard model", *Phys. Rev. D* **42** (1990) 1673, doi:10.1103/PhysRevD.42.1673.

[39] H. Georgi and M. Machacek, "Doubly charged Higgs bosons", *Nucl. Phys. B* **262** (1985) 463, doi:10.1016/0550-3213(85)90325-6.

[40] ATLAS Collaboration, "Search for a charged Higgs boson produced in the vector-boson fusion mode with decay $H^{\pm} \to W^{\pm}Z$ using pp collisions at $\sqrt{s} = 8$ TeV with the ATLAS experiment", *Phys. Rev. Lett.* **114** (2015) 231801, doi:10.1103/PhysRevLett.114.231801, arXiv:1503.04233.

[41] CMS Collaboration, "Search for charged Higgs bosons produced via vector boson fusion and decaying into a pair of W and Z bosons using pp collisions at $\sqrt{s} = 13$ TeV", *Phys. Rev. Lett.* **119** (2017) 141802, doi:10.1103/PhysRevLett.119.141802, arXiv:1705.02942.

[42] CMS Collaboration, "Observation of electroweak production of same-sign W boson pairs in the two jet and two same-sign lepton final state in proton-proton collisions at $\sqrt{s} = 13$ TeV", *Phys. Rev. Lett.* **120** (2018) 081801, doi:10.1103/PhysRevLett.120.081801, arXiv:1709.05822.

[43] CMS Collaboration, "Search for charged Higgs bosons produced in vector boson fusion processes and decaying into vector boson pairs in proton-proton collisions at $\sqrt{s} = 13$ TeV", *Eur. Phys. J. C* **81** (2021) 723, doi:10.1140/epjc/s10052-021-09472-3, arXiv:2104.04762.

[44] ATLAS Collaboration, "Search for dijet resonances in events with an isolated charged lepton using $\sqrt{s} = 13$ TeV proton-proton collision data collected by the ATLAS detector", *JHEP* **06** (2020) 151, doi:10.1007/JHEP06(2020)151, arXiv:2002.11325.

[45] DELPHI, OPAL, ALEPH, L3 and LEP Working Group for Higgs Boson Searches Collaboration, "Search for neutral MSSM Higgs bosons at LEP", *Eur. Phys. J. C* **47** (2006) 547, doi:10.1140/epjc/s2006-02569-7, arXiv:hep-ex/0602042.

[46] CDF Collaboration, "Search for Higgs bosons predicted in Two-Higgs-Doublet models via decays to tau lepton pairs in 1.96 TeV $p\overline{p}$ collisions", *Phys. Rev. Lett.* **103** (2009) 201801, doi:10.1103/PhysRevLett.103.201801, arXiv:0906.1014.

[47] D0 Collaboration, "Search for neutral Higgs bosons in the multi-b-jet topology in 5.2 fb^{-1} of $p\overline{p}$ collisions at $\sqrt{s} = 1.96$ TeV", *Phys. Lett. B* **698** (2011) 97, doi:10.1016/j.physletb.2011.02.062, arXiv:1011.1931.

[48] D0 Collaboration, "Search for Higgs bosons decaying to $\tau^+\tau^-$ pairs in $p\overline{p}$ collisions at $\sqrt{s} = 1.96$ TeV", *Phys. Lett. B* **707** (2012) 323, doi:10.1016/j.physletb.2011.12.050, arXiv:1106.4555.

[49] CDF Collaboration, "Search for Higgs bosons produced in association with b-quarks", *Phys. Rev. D* **85** (2012) 032005, doi:10.1103/PhysRevD.85.032005, arXiv:1106.4782.

[50] CMS Collaboration, "Search for a Higgs boson decaying into a b-quark pair and produced in association with b quarks in proton-proton collisions at 7 TeV", *Phys. Lett. B* **722** (2013) 207, doi:10.1016/j.physletb.2013.04.017, arXiv:1302.2892.

[51] CMS Collaboration, "Search for neutral MSSM Higgs bosons decaying into a pair of bottom quarks", *JHEP* **11** (2015) 071, doi:10.1007/JHEP11(2015)071, arXiv:1506.08329.

[52] CMS Collaboration, "Search for beyond the standard model Higgs bosons decaying into a $b\bar{b}$ pair in pp collisions at $\sqrt{s} = 13$ TeV", *JHEP* **08** (2018) 113, doi:10.1007/JHEP08(2018)113, arXiv:1805.12191.

[53] ATLAS Collaboration, "Search for heavy neutral Higgs bosons produced in association with b-quarks and decaying into b-quarks at $\sqrt{s} = 13$ TeV with the ATLAS detector", *Phys. Rev. D* **102** (2020) 032004, doi:10.1103/PhysRevD.102.032004, arXiv:1907.02749.

[54] ATLAS Collaboration, "Search for the neutral Higgs bosons of the minimal supersymmetric standard model in pp collisions at $\sqrt{s} = 7$ TeV with the ATLAS detector", *JHEP* **02** (2013) 095, doi:10.1007/JHEP02(2013)095, arXiv:1211.6956.

[55] CMS Collaboration, "Search for neutral MSSM Higgs bosons decaying to $\mu^+\mu^-$ in pp collisions at $\sqrt{s} = 7$ and 8 TeV", *Phys. Lett. B* **752** (2016) 221, doi:10.1016/j.physletb.2015.11.042, arXiv:1508.01437.

[56] CMS Collaboration, "Search for MSSM higgs bosons decaying to $\mu^+\mu^-$ in proton-proton collisions at $\sqrt{s} = 13$ TeV", *Phys. Lett. B* **798** (2019) 134992, doi:10.1016/j.physletb.2019.134992, arXiv:1907.03152.

[57] ATLAS Collaboration, "Search for scalar resonances decaying into $\mu^+\mu^-$ in events with and without b-tagged jets produced in proton-proton collisions at $\sqrt{s} = 13$ TeV with the ATLAS detector", *JHEP* **07** (2019) 117, doi:10.1007/JHEP07(2019)117, arXiv:1901.08144.

[58] ATLAS Collaboration, "Search for neutral Higgs bosons of the minimal supersymmetric standard model in pp collisions at $\sqrt{s} = 8$ TeV with the ATLAS detector", *JHEP* **11** (2014) 056, doi:10.1007/JHEP11(2014)056, arXiv:1409.6064.

[59] ATLAS Collaboration, "Search for minimal supersymmetric standard model Higgs bosons H/A and for a Z′ boson in the $\tau\tau$ final state produced in pp collisions at $\sqrt{s} = 13$ TeV with the ATLAS detector", *Eur. Phys. J. C* **76** (2016) 585, doi:10.1140/epjc/s10052-016-4400-6, arXiv:1608.00890.

[60] ATLAS Collaboration, "Search for additional heavy neutral Higgs and gauge bosons in the ditau final state produced in 36 fb^{-1} of pp collisions at $\sqrt{s} = 13$ TeV with the ATLAS detector", *JHEP* **01** (2018) 055, doi:10.1007/JHEP01(2018)055, arXiv:1709.07242.

[61] CMS Collaboration, "Search for neutral minimal supersymmetric standard model Higgs bosons decaying to tau pairs in pp collisions at $\sqrt{s} = 7$ TeV", *Phys. Rev. Lett.* **106** (2011) 231801, doi:10.1103/PhysRevLett.106.231801, arXiv:1104.1619.

[62] CMS Collaboration, "Search for neutral Higgs bosons decaying to tau pairs in pp collisions at $\sqrt{s} = 7$ TeV", *Phys. Lett. B* **713** (2012) 68, doi:10.1016/j.physletb.2012.05.028, arXiv:1202.4083.

[63] CMS Collaboration, "Search for neutral MSSM Higgs bosons decaying to a pair of tau leptons in pp collisions", *JHEP* **10** (2014) 160, doi:10.1007/JHEP10(2014)160, arXiv:1408.3316.

[64] CMS Collaboration, "Search for additional neutral MSSM higgs bosons in the $\tau\tau$ final state in proton-proton collisions at $\sqrt{s} = 13\,\text{TeV}$", *JHEP* **09** (2018) 007, doi:10.1007/JHEP09(2018)007, arXiv:1803.06553.

[65] ATLAS Collaboration, "Search for heavy Higgs bosons decaying into two tau leptons with the ATLAS detector using pp collisions at $\sqrt{s} = 13\,\text{TeV}$", *Phys. Rev. Lett.* **125** (2020) 051801, doi:10.1103/PhysRevLett.125.051801, arXiv:2002.12223.

[66] A. Cordero et al., "Dark Matter Signals at the LHC from a 3HDM", *JHEP* **05** (2018) 030, doi:10.1007/JHEP05(2018)030, arXiv:1712.09598.

[67] A. Cordero-Cid et al., "Lepton collider indirect signatures of dark CP-violation", *Eur. Phys. J. C* **80** (2020) 135, doi:10.1140/epjc/s10052-020-7689-0, arXiv:1812.00820.

[68] V. Keus, S. F. King, S. Moretti, and K. Yagyu, "CP Violating Two-Higgs-Doublet Model: Constraints and LHC Predictions", *JHEP* **04** (2016) 048, doi:10.1007/JHEP04(2016)048, arXiv:1510.04028.

[69] K. Kainulainen et al., "On the validity of perturbative studies of the electroweak phase transition in the Two Higgs Doublet model", *JHEP* **06** (2019) 075, doi:10.1007/JHEP06(2019)075, arXiv:1904.01329.

[70] V. Keus, N. Koivunen, and K. Tuominen, "Singlet scalar and 2HDM extensions of the Standard Model: CP-violation and constraints from $(g-2)_\mu$ and eEDM", *JHEP* **09** (2018) 059, doi:10.1007/JHEP09(2018)059, arXiv:1712.09613.

[71] CMS Collaboration, "Performance of the CMS Level-1 trigger in proton-proton collisions at $\sqrt{s} = 13\,\text{TeV}$", *JINST* **15** (2020) P10017, doi:10.1088/1748-0221/15/10/P10017, arXiv:2006.10165.

[72] CMS Collaboration, "The CMS trigger system", *JINST* **12** (2017) P01020, doi:10.1088/1748-0221/12/01/P01020, arXiv:1609.02366.

[73] CMS Collaboration, "The CMS experiment at the CERN LHC", *JINST* **3** (2008) S08004, doi:10.1088/1748-0221/3/08/S08004.

[74] J. Alwall et al., "The automated computation of tree-level and next-to-leading order differential cross sections, and their matching to parton shower simulations", *JHEP* **07** (2014) 079, doi:10.1007/JHEP07(2014)079, arXiv:1405.0301.

[75] P. Artoisenet, R. Frederix, O. Mattelaer, and R. Rietkerk, "Automatic spin-entangled decays of heavy resonances in Monte Carlo simulations", *JHEP* **03** (2013) 015, doi:10.1007/JHEP03(2013)015, arXiv:1212.3460.

[76] P. Nason, "A new method for combining NLO QCD with shower Monte Carlo algorithms", *JHEP* **11** (2004) 040, doi:10.1088/1126-6708/2004/11/040, arXiv:hep-ph/0409146.

[77] S. Frixione, P. Nason, and C. Oleari, "Matching NLO QCD computations with parton shower simulations: the POWHEG method", *JHEP* **11** (2007) 070, doi:10.1088/1126-6708/2007/11/070, arXiv:0709.2092.

[78] S. Alioli, P. Nason, C. Oleari, and E. Re, "A general framework for implementing NLO calculations in shower monte carlo programs: the POWHEG BOX", *JHEP* **06** (2010) 043, doi:10.1007/JHEP06(2010)043, arXiv:1002.2581.

[79] S. Alioli et al., "Jet pair production in POWHEG", *JHEP* **04** (2011) 081, doi:10.1007/JHEP04(2011)081, arXiv:1012.3380.

[80] S. Alioli, P. Nason, C. Oleari, and E. Re, "NLO Higgs boson production via gluon fusion matched with shower in POWHEG", *JHEP* **04** (2009) 002, doi:10.1088/1126-6708/2009/04/002, arXiv:0812.0578.

[81] E. Bagnaschi, G. Degrassi, P. Slavich, and A. Vicini, "Higgs production via gluon fusion in the POWHEG approach in the SM and in the MSSM", *JHEP* **02** (2012) 088, doi:10.1007/JHEP02(2012)088, arXiv:1111.2854.

[82] M. Czakon and A. Mitov, "Top++: A program for the calculation of the top-pair cross-section at hadron colliders", *Comput. Phys. Commun.* **185** (2014) doi:10.1016/j.cpc.2014.06.021, arXiv:1112.5675.

[83] R. Frederix, E. Re, and P. Torrielli, "Single-top *t*-channel hadroproduction in the four-flavour scheme with POWHEG and aMC@NLO", *JHEP* **09** (2012) 130, doi:10.1007/JHEP09(2012)130, arXiv:1207.5391.

[84] E. Re, "Single-top Wt-channel production matched with parton showers using the POWHEG method", *Eur. Phys. J. C* **71** (2011) 1547, doi:10.1140/epjc/s10052-011-1547-z, arXiv:1009.2450.

[85] H. B. Hartanto, B. Jager, L. Reina, and D. Wackeroth, "Higgs boson production in association with top quarks in the POWHEG BOX", *Phys. Rev. D* **91** (2015) 094003, doi:10.1103/PhysRevD.91.094003, arXiv:1501.04498.

[86] T. Sjöstrand et al., "An introduction to PYTHIA 8.2", *Comput. Phys. Commun.* **191** (2015) 159, doi:10.1016/j.cpc.2015.01.024, arXiv:1410.3012.

[87] J. Alwall et al., "Comparative study of various algorithms for the merging of parton showers and matrix elements in hadronic collisions", *Eur. Phys. J. C* **53** (2008) 473, doi:10.1140/epjc/s10052-007-0490-5, arXiv:0706.2569.

[88] R. Frederix and S. Frixione, "Merging meets matching in MC@NLO", *JHEP* **12** (2012) 061, doi:10.1007/JHEP12(2012)061, arXiv:1209.6215.

[89] NNPDF Collaboration, "Parton distributions for the LHC Run II", *JHEP* **04** (2015) 040, doi:10.1007/JHEP04(2015)040, arXiv:1410.8849.

[90] NNPDF Collaboration, "Parton distributions from high-precision collider data", *Eur. Phys. J. C* **77** (2017) 663, doi:10.1140/epjc/s10052-017-5199-5, arXiv:1706.00428.

[91] CMS Collaboration, "Event generator tunes obtained from underlying event and multiparton scattering measurements", *Eur. Phys. J. C* **76** (2016) 155, doi:10.1140/epjc/s10052-016-3988-x, arXiv:1512.00815.

[92] CMS Collaboration, "Extraction and validation of a new set of CMS Pythia8 tunes from underlying-event measurements", *Eur. Phys. J. C* **80** (2020) 4, doi:10.1140/epjc/s10052-019-7499-4.

[93] GEANT4 Collaboration, "GEANT4—a simulation toolkit", *Nucl. Instrum. Meth. A* **506** (2003) 250, doi:10.1016/S0168-9002(03)01368-8.

[94] CMS Collaboration, "Particle-flow reconstruction and global event description with the CMS detector", *JINST* **12** (2017) P10003, doi:10.1088/1748-0221/12/10/P10003, arXiv:1706.04965.

[95] M. Cacciari, G. P. Salam, and G. Soyez, "The anti-k_{T} jet clustering algorithm", *JHEP* **04** (2008) 063, doi:10.1088/1126-6708/2008/04/063, arXiv:0802.1189.

[96] M. Cacciari, G. P. Salam, and G. Soyez, "FastJet user manual", *Eur. Phys. J. C* **72** (2012) 1896, doi:10.1140/epjc/s10052-012-1896-2, arXiv:1111.6097.

[97] CMS Collaboration, "Electron and photon reconstruction and identification with the CMS experiment at the CERN LHC", *JINST* **16** (2021) P05014, doi:10.1088/1748-0221/16/05/P05014, arXiv:2012.06888.

[98] CMS Collaboration, "Performance of the CMS muon detector and muon reconstruction with proton-proton collisions at $\sqrt{s} = 13\,\mathrm{TeV}$", *JINST* **13** (2018) P06015, doi:10.1088/1748-0221/13/06/P06015, arXiv:1804.04528.

[99] CMS Collaboration, "Pileup mitigation at CMS in 13 TeV data", *JINST* **15** (2020) P09018, doi:10.1088/1748-0221/15/09/P09018, arXiv:2003.00503.

[100] CMS Collaboration, "Jet energy scale and resolution in the CMS experiment in pp collisions at 8 TeV", *JINST* **12** (2017) P02014, doi:10.1088/1748-0221/12/02/P02014, arXiv:1607.03663.

[101] E. Bols et al., "Jet flavour classification using DeepJet", *JINST* **15** (2020) P12012, doi:10.1088/1748-0221/15/12/P12012, arXiv:2008.10519.

[102] CMS Collaboration, "Performance of the DeepJet b tagging algorithm using 41.9 fb^{-1} of data from proton-proton collisions at 13 TeV with Phase 1 CMS detector", CMS Detector Performance Note CMS-DP-2018-058, 2018.

[103] CMS Collaboration, "Identification of heavy-flavour jets with the CMS detector in pp collisions at 13 TeV", *JINST* **13** (2018) P05011, doi:10.1088/1748-0221/13/05/P05011, arXiv:1712.07158.

[104] CMS Collaboration, "Performance of reconstruction and identification of τ leptons decaying to hadrons and ν_τ in pp collisions at $\sqrt{s} = 13\,\mathrm{TeV}$", *JINST* **13** (2018) P10005, doi:10.1088/1748-0221/13/10/P10005, arXiv:1809.02816.

[105] CMS Collaboration, "Identification of hadronic tau lepton decays using a deep neural network", 2022. arXiv:2201.08458. Submitted to *JINST*.

[106] CMS Collaboration, "Performance of the DeepTau algorithm for the discrimination of taus against jets, electron, and muons", CMS Detector Performance Note CMS-DP-2019-033, 2019.

[107] CMS Collaboration, "Performance of missing transverse momentum reconstruction in proton-proton collisions at $\sqrt{s} = 13\,\mathrm{TeV}$ using the CMS detector", *JINST* **14** (2019) P07004, doi:10.1088/1748-0221/14/07/P07004, arXiv:1903.06078.

[108] F. Chollet et al., "Keras". https://keras.io, 2015.

[109] M. Abadi et al., "TensorFlow: Large-scale machine learning on heterogeneous systems", 2015. arXiv:1603.04467. Software available from tensorflow.org.

[110] F. Pedregosa et al., "Scikit-learn: Machine learning in Python", *J. Mach. Learn. Res.* **12** (2011) 2825, arXiv:1201.0490.

[111] CMS Collaboration, "Measurement of the $Z/\gamma^* \to \tau\tau$ cross section in pp collisions at $\sqrt{s} = 13$ TeV and validation of τ lepton analysis techniques", *Eur. Phys. J. C* **78** (2018) 708, doi:10.1140/epjc/s10052-018-6146-9, arXiv:1801.03535.

[112] H. Voss, A. Höcker, J. Stelzer, and F. Tegenfeldt, "TMVA, the toolkit for multivariate data analysis with ROOT", in *XIth International Workshop on Advanced Computing and Analysis Techniques in Physics Research (ACAT)*, p. 40. 2007. arXiv:physics/0703039. [PoS(ACAT)040]. doi:10.22323/1.050.0040.

[113] R. J. Barlow and C. Beeston, "Fitting using finite Monte Carlo samples", *Comput. Phys. Commun.* **77** (1993) 219, doi:10.1016/0010-4655(93)90005-W.

[114] J. S. Conway, "Incorporating Nuisance Parameters in Likelihoods for Multisource Spectra", in *PHYSTAT 2011*. 3, 2011. arXiv:1103.0354. doi:10.5170/CERN-2011-006.115.

[115] CMS Collaboration, "Precision luminosity measurement in proton-proton collisions at $\sqrt{s} = 13$ TeV in 2015 and 2016 at CMS", *Eur. Phys. J. C* **81** (2021) 800, doi:10.1140/epjc/s10052-021-09538-2, arXiv:2104.01927.

[116] CMS Collaboration, "CMS luminosity measurement for the 2017 data-taking period at $\sqrt{s} = 13$ TeV", CMS Physics Analysis Summary CMS-PAS-LUM-17-004, 2018.

[117] CMS Collaboration, "CMS luminosity measurement for the 2018 data-taking period at $\sqrt{s} = 13$ TeV", CMS Physics Analysis Summary CMS-PAS-LUM-18-002, 2019.

[118] ATLAS Collaboration, "Measurement of the inelastic proton-proton cross section at $\sqrt{s} = 13$ TeV with the ATLAS detector at the LHC", *Phys. Rev. Lett.* **117** (2016) 182002, doi:10.1103/PhysRevLett.117.182002, arXiv:1606.02625.

[119] CMS Collaboration, "Measurement of the inelastic proton-proton cross section at $\sqrt{s} = 13$ TeV", *JHEP* **07** (2018) 161, doi:10.1007/JHEP07(2018)161, arXiv:1802.02613.

[120] LHC Higgs Cross Section Working Group, "Handbook of LHC Higgs Cross Sections: 3. Higgs Properties", *CERN Yellow Rep. Monogr.* **4** (2013) doi:10.5170/CERN-2013-004, arXiv:1307.1347.

[121] LHC Higgs Cross Section Working Group, "Handbook of LHC Higgs Cross Sections: 4. Deciphering the nature of the Higgs sector", *CERN Yellow Rep. Monogr.* **2** (2017) doi:10.23731/CYRM-2017-002, arXiv:1610.07922.

[122] J. Butterworth et al., "PDF4LHC recommendations for LHC Run II", *J. Phys. G* **43** (2016) 023001, doi:10.1088/0954-3899/43/2/023001, arXiv:1510.03865.

[123] HEPData record for this analysis, 2022. doi:10.17182/hepdata.130491.

[124] T. Junk, "Confidence level computation for combining searches with small statistics", *Nucl. Instrum. Meth. A* **434** (1999) doi:10.1016/S0168-9002(99)00498-2, arXiv:hep-ex/9902006.

[125] A. L. Read, "Presentation of search results: The CL_s technique", *J. Phys. G* **28** (2002) 2693, doi:10.1088/0954-3899/28/10/313.

[126] CMS Collaboration, "Combined results of searches for the standard model Higgs boson in pp collisions at $\sqrt{s} = 7\,\text{TeV}$", *Phys. Lett. B* **710** (2012) 26, doi:10.1016/j.physletb.2012.02.064, arXiv:1202.1488.

[127] G. Cowan, K. Cranmer, E. Gross, and O. Vitells, "Asymptotic formulae for likelihood-based tests of new physics", *Eur. Phys. J. C* **71** (2011) 1554, doi:10.1140/epjc/s10052-011-1554-0, arXiv:1007.1727. [Erratum: doi:10.1140/epjc/s10052-013-2501-z].